STRUCTURAL AND MAGNETIC STUDIES

STRUCTURAL AND MAGNETIC STUDIES
ON RARE-EARTH SUPERLATTICES PREPARED
BY MOLECULAR BEAM EPITAXY TECHNIQUE

分子線エピタキシー法により作製した
希土類金属超格子の構造と磁性に関する研究

ATSUSHI MAEDA

前田篤志

STRUCTURAL AND MAGNETIC STUDIES ON RARE-EARTH SUPERLATTICES PREPARED BY MOLECULAR BEAM EPITAXY TECHNIQUE

by

Atsushi Maeda

A Thesis Submitted to the University of Tokyo
for the Degree of Doctor of Science
(Rigaku Hakushi)

March, 1992

This thesis was written principally based on the papers already published as listed below.

[1] ·Dipole-Dipole Interaction in the Diffused Interlayer of Magnetic Superlattices
·Atsushi Maeda and Haruo Kuroda
·Thin Solid Films, 161, L83 (1988)

[2] ·Structural and Magnetic Studies of an Artificial Eu/Mn Superlattice
·Atsushi Maeda, Tohru Satake, Toshinari Fujimori, Hiroyuki Tajima, Mototada Kobayashi and Haruo Kuroda
·Journal of Applied Physics, 65, 3845 (1989)

[3] ·Magnetic-Frozen States in Eu/Mn Superlattices
·Atsushi Maeda, Tohru Satake, Toshinari Fujimori and Haruo Kuroda
·Journal of Physics, 2, 245 (1990)

[4] ·体心立方Ｅｕ／Ｙｂ超格子のエピタキシャル成長
－ Ｙｂ金属高温相の安定化 －
·前田篤志，佐竹徹，藤森俊成，黒田晴雄
·日本応用磁気学会誌，14, 359 (1990)

[5] ·Structural and Magnetic Characteristics of Eu/Mn and Eu/Yb Superlattices Prepared by the MBE Technique
·Atsushi Maeda, Tohru Satake, Toshinari Fujimori and Haruo Kuroda
·Vacuum, 41, 1251 (1990)

[6] ·Epitaxial Growth of bcc-Eu/Yb Superlattices
·Atsushi Maeda, Tohru Satake, Toshinari Fujimori and Haruo Kuroda
·Journal of Applied Physics, 68, 3246 (1990)

[7] ·In Situ Electron Beam Irradiation Induced In-Plane Orientation of Europium Thin Film Grown by the Molecular Beam Epitaxy Technique
·Atsushi Maeda, Tohru Satake, Toshinari Fujimori, Shigeru Maeda and Haruo Kuroda
·Thin Solid Films, 192, 135 (1990)

[8] ·Thermal Hysteresis Phenomena in Eu/Yb Superlattices
·Atsushi Maeda, Tohru Satake, Toshinari Fujimori and Haruo Kuroda
·Journal of Physics, 3, 1967 (1991)

[9] ·Ｄｙ／Ｙｂ人工格子の構造と磁性
·前田篤志，佐竹徹，藤森俊成，黒田晴雄
·日本応用磁気学会誌，15, 441 (1991)

[10] ·Epitaxial Growth of fcc-Sm/Yb Artificial Superlattices
·Atsushi Maeda, Tohru Satake, Toshinari Fujimori and Haruo Kuroda
·Journal of Applied Physics, 69, 6417 (1991)

[11] ·Spin-Reorientation Phenomena in Dy/Yb Superlattices
·Atsushi Maeda, Tohru Satake and Haruo Kuroda
·Journal of Physics, 3, 5241 (1991)

[12] ·Magnetic-Field Dependence of Eu/Mn Superlattices
·Atsushi Maeda, Tohru Satake and Haruo Kuroda
·Physics Letters A, 157, 178 (1991)

ACKNOWLEDGEMENT

The present study has been conducted under the guidance of Professor Haruo Kuroda (Univ. of Tokyo). The author wishes to thank him for his continuing interest, valuable discussions, and encouragement.

The author is sincerely grateful to Dr. Tohru Satake (Ebara Research Co., Ltd.) and Mr. Toshinari Fujimori (Mitsubishi Kasei Corp.) for their help with experiments and useful discussions.

The author gratefully acknowledges Mr. Atsuo Mizukami (Sanyo Electric Co., Ltd.) and Dr. Satoshi Hanai (Mitsubishi Corp.) for their encouragement during this work.

The author thanks Professor Akira Kinbara (Univ. of Tokyo), Professor Hiroumi Ishii (Osaka City Univ.), and Dr. Tetsuya Sato (Keio Univ.) for their valuable discussions.

The author is indebted to Dr. Robert M. Lewis (Tsukuba Research Consortium) for his useful discussion and critical reading of the manuscript. The author is also grateful to Professor Mototada Kobayashi (Himeji Institute of Tech.), Dr. Hiroyuki Tajima (Univ. of Tokyo), Dr. Shigeru Maeda (Nippon Steel Corp.), Dr. Takeji Takui (Osaka City Univ.) and Mr. Hironobu Takahashi (Sanyo Electric Co., Ltd.) for their helpful discussions.

Dr. Michiko Kusunoki (Meijyo Univ.) and Dr. Retsu Oiwa (Ulvac Phi, Inc.) are gratefully acknowledged for their help

with transmission electron diffraction and Auger electron spectroscopy measurements, respectively.

CONTENTS

CHAPTER I

GENERAL INTRODUCTION

1. Metallic Superlattices: Past and Present

The history of research on metallic superlattices is rather long. The initial purpose of preparing metallic superlattices was to fabricate periodic structures with wavelengths not available in the lattice spacings of natural crystals. The first known attempt to make a superlattice appears to have been made by Deubner. He made Au/Ag and Ag/Cu superlattices and was able to observe the diffraction attributable to the composition modulation.[1] DuMond et al. produced a Au/Cu superlattice and observed that the decay of the amplitude of the superlattice-ralated x-ray satellites can be used as a measure of interdiffusion.[2] After these investigations, many workers concentrated on the metallic superlattices for the study of the physics of diffusion.[3-5] However, they measured the characteristics only as diffraction grating for soft x-ray and were not concerned with the physical properties. This is because vacuum technology before the 1970's was not advanced enough to allow reliable samples to be produced, for which the physical properties could be strictly discussed. In 1970, semiconductor superlattice study was initiated by Esaki et al.[6] This triggered an advancement in vacuum technology and deposition techniques. As a result, epitaxial stacking at superlattice interfaces was accomplished and the growth of single crystal superlattices became possible in the semiconductor field, as typified by the GaAs-AlGaAs system.[7] On the other hand, there were few reports on epitaxial metallic superlattices in those days. In 1981 high-energy ion-scattering measurements indicated that the Ag/Au superlattice is grown on Ag (111) layer by layer.[8] This is the first example that showed the possibility of fabricating by the molecular beam deposition a single-crystal superlattice comprising transition metals. The discovery that single-crystal films of Y can be grown epitaxially on Nb layer led to the synthesis of the first single-crystal rare-earth superlattices, Gd/Y.[9] Thus, fundamental research on the physical properties of metallic superlattices has advanced considerably by now.

Much of the early work on the physics of metallic superlattices was concerned with superconductivity. This is because the coherence length of typical superconductors is very long, with dimensional effects already appearing in films with a thickness of several 100 Å. This means that layering on an atomic-scale is not required for research on dimensional crossover phenomena. From this point of view, metallic superlattices are useful specimens for the investigation of basic parameters in superconductivity physics, such as coherence length, penetration depth, and proximity effect. Only the Nb-based systems received systematic study as part of the current interest in synthetically layered materials. High-quality Nb/Ge superlattices prepared by sputter deposition were studied by Ruggiero et al.[10] Their primary motivation was to study dimensional crossover effects in quasi-two-dimensional superconductors. The Nb/Ge superlattices proved highly successful in this regard because the degree of interlayer coupling could be adequately controlled by varying the Ge thickness. Nb/Cu,[11] Nb/Ti,[12] Nb/Zr,[13] and Nb/Al[14] superlattices also received considerable experimental attention to date. However, the discovery of high temperature superconductivity in metallic oxides, such as $YBa_2Cu_3O_x$,[15] $Bi_2Sr_2CaCu_2O_x$,[16] and $Tl_2Ba_2Ca_2Cu_3O_x$,[17] has clearly changed the focus of the field of superconducting superlattices. Although superconductivity in these oxides is not yet well understood, it appears likely that the layered nature of these materials plays an important role in their physical properties and possibly even in the existence of superconductivity itself. Therefore, it is expected that the understanding of superconductivity gained by the study of superlattice superconductors is applicable to these new materials. More importantly, the design and preparation principles for superconducting superlattices may find application at an atomic-level to the synthesis of these oxides. Very recently, Triscone et al. studied the superconductivity in superlattices containing $YBa_2Cu_3O_7$ layers separated by insulating $PrBa_2Cu_3O_7$ layers.[18] A linear reduction of T_C was observed with increasing thickness of the $PrBa_2Cu_3O_7$ layer, suggesting that a minimum interlayer coupling is necessary for superconductivity to occur in the individual $YBa_2Cu_3O_7$ layers.

Magnetism is another basic physical property of metallic systems. Already we have fairly well recognized the magnetic properties of bulk metals. On the other hand, our knowledge on the magnetic properties of surfaces and interfaces is not yet sufficient. Liebermann et al. measured the magnetization of Fe, Co, and Ni thin films as a function of thickness and explained the results by assuming that the first surface layer has no magnetic moment.[19] In contrast, Freeman's group systematically carried out the theoretical calculation of electronic and magnetic structures in Fe, Co, and Ni thin films with the thickness of several monolayers.[20] The theoretical results suggested some increase of surface magnetic moments and refuted the existence of "dead" layer. The disagreement between experimental and theoretical studies is because that the experimental technique has not been advanced enough to evaluate the magnetic property of monolayer or interface. Here superlattice samples have a definite merit for the study of monolayer or interface magnetism. Namely, by using superlattices including two orders more monolayers, we can apply any conventional techniques for the characterization of monolayer or interface magnetism. Using ferromagnetic resonance measurement, Thaler et al. concluded that the magnetic moment of Ni atoms at interface sites in Cu/Ni superlattices is larger than the standard bulk value.[21] Though their result was refuted by the detailed investigation of Gyorgy et al.,[22] Thaler's study increased the interest in the magnetic properties of metallic superlattices. Thus, most studies reported to date on magnetic superlattices have focused on the interface characteristics. Many d-spin superlattices containing ferromagnetic transition metals were prepared in these studies. Hyperfine field measurement using Mö ssbauer spectroscopy is effective to study the interfaces of metallic superlattices. From ^{57}Fe Mö ssbauer measurements, Fe atoms were found to be non-magnetic in the Fe (2 Å)/V (16 Å) superlattice.[23] In contrast, the magnetic interface effect was shown to be small in the Fe/Mg superlattices.[24] That is, Fe atoms contacting with Mg at the interface layer had magnetic moments similar to the bulk value. Moreover, Fe monolayers sandwiched between Mg layers appeared to be ferromagnetic and the local magnetic moments were reduced only slightly. The interface magnetism of superlattices is also very interesting from technological viewpoints. Co/Pd and Co/Pt superlattices with perpendicular magnetizations which are stabilized by the interfacial anisotropy were actively investigated and were reported to be possible candidates for perpendicular magnetic recording media[25] and magneto-optical recording media.[26]

2. Preparation Techniques for Metallic Superlattices

Sputtering is a well-established technique for preparing thin films. The sputtering process entails establishing a plasma discharge and imposing a potential of the correct polarity so that ionized gas atoms are accelerated to a target surface. If the ionized gas atoms are of sufficient energy, atoms and/or clusters are ejected from the solid target into the vapor phase. The ejected atoms impinge on a substrate and condense to form a film. In the system used for superlattice preparation, the sputter sources are widely separated and the substrates moved past the sources, a single layer being deposited on each pass by a source. Here there are several demerits for preparation of superlattices in comparison with vacuum deposition. First, ion bombardment during synthesis provides knock on mixing between layers. This is due to the higher kinetic energy of sputtered atoms. It is also impossible to eliminate the inclusion of inert sputter gas in the growing film. Furthermore, it is difficult to control the substrate temperature because the bombardment by either neutral or ionized inert gas ions results in heating of the substrate. Thus, superlattices with clean interfaces cannot be synthesized using a sputtering method.

Vacuum deposition is also used for the preparation of metallic superlattices. Since the deposition should be slow enough for atomic-scale control, to form flat surfaces, and to prevent interdiffusion, the surface will become contaminated by the adsorption of residual gas from the vacuum chamber. This indicates that ultra-high vacuum is an important condition for superlattice preparation by vacuum deposition. Knudsen cells are used to prepare semiconductor superlattices. The atomic and/or molecular beams generated from Knudsen cells travel, with guidance from orifices and shutters, in linear paths in the vacuum space and condense on the substrate under kinetically favorable conditions. This approach produces superlattices with high-quality. On the other hand, the electron beam (EB) gun is mainly used as the deposition source for metallic systems. Beams made by evaporating substances with EB guns tend to expand. It is also difficult to control the rate of beams generated by EB guns, because the part that is heated is very small, producing a large thermal distribution in the evaporation source. In addition, EB heating often results in significant radiant heating of the substrate which makes substrate temperature control difficult. These demerits of vacuum deposition using EB guns result in inferior superlattice quality.

3. Magnetism of Rare-Earth Metals

For the rare-earth metals, the magnetic moment arises from the partially filled 4f shells of each atom. According to the Russell-Saunders coupling scheme, an unfilled atomic shell carries a total angular momentum, J, and a magnetic moment, $g\mu_B J$. J can be defined as

$$J = L + S \quad \text{or} \quad |L - S|$$

depending on whether the shell is more or less than half filled, respectively, where L is a total orbital angular momentum and S is a total spin angular momentum. For the magnetic moment, μ_B is the Bohr magneton and g, the Landé factor, can be defined as

$$g = 1 + \frac{J(J+1) - L(L+1) + S(S+1)}{2J(J+1)}.$$

Here the 4f charge drops off rapidly and becomes essentially zero at the Wigner-Seitz sphere radius. Therefore, the rare-earth metals were believed to be the best examples of truly local magnetic moment systems. In fact, however, complex magnetic characteristics which cannot be explained by the local model are observed in the rare-earth metals. The 4f magnetic electron wave functions do not in themselves have a significant direct overlap integral and thus the complexity of the magnetism in rare-earth metals lies in the magnetic coupling that occurs via a polarization wave formed in the conduction electron bands. This coupling was based on a suggestion by Zener,[27] and was initially calculated by Ruderman and Kittel for nuclear moments in a free electron gas.[28] Later Kasuya[29] and Yosida[30] provided the formalism describing the now well-known Ruderman-Kittel-Kasuya-Yosida (RKKY) coupling between localized 4f spins. The effective hamiltonian of RKKY interaction is

$$H = \left(\frac{3N_e}{N}\right)^2 \frac{4\pi}{\varepsilon_F} J^2 F(2\kappa_F R_{nm}) S_n \cdot S_m,$$

where

$$F(x) = \frac{x\cos x - \sin x}{x^4},$$

N_e and N are the total number of electrons and atoms, respectively, ε_F the Fermi energy, κ_F the Fermi wave vector, and R_{nm} the distance between the spins S_n and S_m which mutually interact through the polarization of the conduction bands. Here it is extremely important that the interaction has the spatial dependence $\cos(2\kappa_F R_{nm})/R_{nm}^3$ for large distances. The outstanding feature of the coupling energy as a function of distance is the long-range oscillatory behavior. Thus, the spin coupling of 4f magnetic moments involving a polarization wave in the conduction bands is of a very long-range character. At low temperatures, it has been found that the rare-earth metals possess complex magnetic order arising from this RKKY interaction.[31] For example, Gd has the ferromagnetic structure below 293 K, while Tb and Dy first order in a helical structure and make a phase transition to the ferromagnetic structure at low temperatures. Ho orders in a helical structure, then transforms into a conical structure. Er has, in order of decreasing temperature, helical, conical, and longitudinal sinusoidally modulated structures. Tm has longitudinal sinusoidally modulated and antiphase domain structures.

4. Aims of the Present Study

As described in Section 1, the past study on the magnetism of metallic superlattices was aimed at understanding the interface characteristics of superlattices containing ferromagnetic transition metals. It is also extremely interesting to study the effects of reduced dimensionality on the magnetic ground state and the dependence of magnetic properties on the artificial compositional modulation in the superlattice materials. However, the magnetism resulting from such phenomenon in superlattices was not clearly understood in past studies. This may be because the magnetic coupling between the d-spins in the transition metals is only effective over a short-range. Namely, the thickness of magnetic layers in superlattices containing transition metals must be a few atomic-layers to reduce the dimensionality. Similarly, when the interlayer interaction between the magnetic layers is induced in d-spin superlattices, the thickness of intervening layer must be only a few atomic-layers. Unfortunately such atomic-level control is still not possible in the preparation of metallic superlattices, as described in Section 2. In the present study, therefore, the following research aims were set:

(1) Atomic-scale control of metallic superlattice structure.

(2) Confirmation of unique magnetism arising from artificial compositional modulation and reduced dimensionality.

To achieve the first aim, the molecular beam epitaxy (MBE) method which has produced good results in the field of semiconductors was used to prepare metallic superlattices. The MBE method has developed rapidly over the last ten years. The growth of layers involves controlling, via shutters and source temperature, atomic and/or molecular beams directed at a substrate to achieve epitaxial growth. The vacuum needed to minimize contamination is determined by the relatively slow film growth rate of approximately ten Å per minute and is commonly in around 10^{-11} Torr. The mean free path of gases at this pressure and in the beams themselves is several orders of magnitude greater than the normal source-to-substrate distance of a few tens of cm. Hence, the beams impinge unreacted on the substrate (indirect paths to the substrate are minimized by surrounding the substrate with a cryo-shroud cooled by liquid nitrogen). The beams are ideally generated from Knudsen cells in which quasi-thermal equilibrium is maintained. The beams travel, with guidance from orifices and shutters, in linear paths in the vacuum space and condense on the substrate under kinetically favorable conditions. Timely actuation of the source shutters allows film growth to be controlled to the monolayer level. Next, the rare-earth metals were selected as the components of metallic superlattices to achieve the second aim described above. This is because the magnetic coupling between the 4f spins, which is mediated indirectly through the polarization wave in the conduction bands, is effective over a relatively long-range compared to that of d-spin systems, as described in Section 3. This long-range character was expected to allow the second aim to be realized. Namely, isolated arrays of moments which vary both in thickness and in separation can be synthesized as a model system for investigation of intermagnetic layer coupling and two-dimensional magnetism.

The appearance of new physical properties can be expected to result from the structure of metallic superlattices. A well-known example is Fe layers epitaxially grown on a Cu substrate. When the Fe layer thickness was less than about 20 Å, the structure was the fcc (high temperature) phase instead of the bcc (ambient temperature) phase and the ferromagnetism disappeared.[32] Brodsky also reported that a thin Cr layer sandwiched between Au layers has an fcc structure.[33] Normally Cr metal has a bcc structure and exhibits antiferromagnetic properties. In contrast, the epitaxial fcc-Cr showed superconducting behavior below 4 K. These studies indicate that the high temperature and/or high pressure metal phases can be stabilized using the epitaxial relationship at superlattice interfaces. Namely, when the lattice constant of the high temperature phase, bcc for example, of metal X is very close to that of the ambient temperature bcc phase of metal Y, epitaxial growth of metal X on metal Y is expected to produce the bcc structure of metal X. The high temperature phase of metal X thus prepared may be stabilized by being sandwiched between two layers of metal Y. The unknown magnetic and/or electronic properties of such artificial crystals are very interesting, as described for Fe and Cr metals. In the present study, therefore, the following is also set as one of the research aims:

(3) Stabilization of non-thermodynamic metal phases using the epitaxial relationship at superlattice interfaces.

5. Contents of the Present Thesis

This Doctor's thesis is organized into seven chapters, including this chapter and two appendixes. Chapter II is an overview of experimental procedures used in the present study. In this chapter, the MBE apparatus specially designed for this study is described in detail. In addition, the characterization techniques for the metallic superlattices are presented. In Chapters III, IV, V, and VI, the structural and magnetic characteristics of Eu/Mn, Eu/Yb, Dy/Yb, and Sm/Yb superlattices, respectively, are described. The unique magnetic behavior associated with superperiodicity is mainly discussed in Chapters III, V, and part of IV. Chapter VI and part of Chapter IV deal with the crystal growth of non-thermodynamic rare-earth metal phases. The conclusion on the structural and magnetic properties of rare-earth metal superlattices are given in the last chapter, Chapter VII. In Appendix I, published papers which are directly related to the present study are listed. Appendix II deals with other papers published.

References

[1] W. Deubner, Annin. Phys., 5, 261 (1930).

[2] J. DuMond and J. P. Youtz, J. Appl. Phys., 11, 357 (1940).

[3] J. B. Dinklage and R. Frerichs, J. Appl. Phys., 34, 2633 (1967).

[4] J. B. Dinklage, J. Appl. Phys., 38, 3781 (1967).

[5] H. E. Cook and J. E. Hilliard, J. Appl. Phys., 40, 2191 (1969).

[6] L. Esaki and R. Tsu, IBM J. Res. Dev., 14, 61 (1970).

[7] L. L. Chang, L. Esaki, W. E. Howard and R. Ludeke, J. Vac. Sci. Technol., 10, 11 (1973).

[8] R. J. Culbertson, L. C. Feldman, P. J. Silverman and H. Boehm, Phys. Rev. Lett., 47, 657 (1981).

[9] J. Kwo, E. M. Gyorgy, D. B. McWhan, M. Hong, F. J. DiSalvo, C. Vettier and J. E. Bower, Phys. Rev. Lett., 55, 1402 (1985).

[10] S. T. Ruggiero, T. W. Barbee, Jr. and M. R. Beasley, Phys. Rev. Lett., 45, 1299 (1980).

[11] I. K. Schuller, Phys. Rev. Lett., 44, 1597 (1980).

[12] J. Q. Zheng, J. B. Ketterson, C. M. Falco and I. K. Schuller, Physica B 108, 945 (1981).

[13] W. P. Lowe and T. H. Geballe, Phys. Rev. B 29, 4961 (1984).

[14] J. Geerk, M. Gurvitch, D. B. McWhan and J. M. Rowell, Physica B 109-110, 1775 (1982).

[15] M. K. Wu, J. R. Ashburn, C. T. Torng, P. H. Hor, R. L. Meng, L. Gao, Z. J. Huang, Y. Q. Wang and C. W. Chu, Phys. Rev. Lett., 58, 908 (1987).

[16] H. Maeda, Y. Tanaka, M. Fukutomi and T. Asano, Jpn. J. Appl. Phys., 27, L209 (1988).

[17] R. M. Hazen, L. W. Finger, R. J. Angel, C. T. Prewit, N. L. Ross, C. G. Hadidiacos, P. J. Heaney, D. R. Veblen, Z. Z. Sheng, A. Elali and A. M. Hermann, Phys. Rev. Lett., 60, 1657 (1988).

[18] J.-M. Triscone, ϕ . Fischer, O. Brunner, L. Antognazza, A. D. Kent and M. G. Karkut, Phys. Rev. Lett., 64, 804 (1990).

[19] L. N. Liebermann, D. R. Fredkin and H. B. Shore, Phys. Rev. Lett., 22, 539 (1969); L. N. Liebermann, J. Clinton, D. M. Edwards and J. Mathon, Phys. Rev. Lett., 25, 232 (1970).

[20] S. Ohnishi, A. J. Freeman and M. Weinert, Phys. Rev. B 28, 6741 (1983); E. Wimmer, A. J. Freeman and H. Krakauer, Phys. Rev. B 30, 3113 (1984); L. I. Chu, A. J. Freeman and C. L. Fu, J. Magn. Magn. Mater., 75, 53 (1988).

[21] B. J. Thaler, J. B. Ketterson and J. E. Hilliard, Phys. Rev. Lett., 41, 336 (1978).

[22] E. M. Gyorgy, D. B. McWhan, J. E. Dillon, Jr., L. R. Walker and J. V. Waszczak, Phys. Rev. B 25, 6739 (1982).

[23] N. Hosoito, K. Kawaguchi, T. Shinjo, T. Takada and Y. Endoh, J. Phys. Soc. Jpn., 53, 2659 (1984).

[24] K. Kawaguchi, R. Yamamoto, N. Hosoito, T. Shinjo and T. Takada, J. Phys. Soc. Jpn., 55, 2375 (1986).

[25] P. F. Carcia, A. D. Meinhaldt and A. Suna, Appl. Phys. Lett., 47, 178 (1985).

[26] Y. Ochiai, S. Hashimoto and K. Aso, Jpn. J. Appl. Phys., 28, L659 (1989).

[27] C. Zener, Phys. Rev., 81, 446 (1951).

[28] M. Ruderman and C. Kittel, Phys. Rev., 96, 99 (1954).

[29] T. Kasuya, Prog. Theor. Phys., 16, 45 (1956).

[30] K. Yosida, Phys. Rev., 106, 893 (1957).

[31] S. H. Liu, in Handbook of the Physics and Chemistry of the Rare Earths, edited by K. A. Gschneidner, Jr. and L. Eyring (North-Holland, Amsterdam, 1978), Vol. 1, p. 233-336.

[32] R. Halbauer and U. Gonser, J. Magn. Magn. Mater., 35, 55 (1983).

[33] M. B. Brodsky, P. Marikar, R. J. Friddle, L. Singer and C. H. Sowers, Solid State Commun., 42, 675 (1982).

CHAPTER II

EXPERIMENTAL

1. Preparation

The MBE apparatus (ULVAC original design) used for the preparation of metallic superlattices in the present study is shown schematically in Figure 1. The chambers were fabricated from stainless steel and all chamber ports were sealed with copper gaskets. The preparation chamber was evacuated to 5×10^{-10} Torr by a rotary pump and a turbo molecular pump. This chamber can hold four substrates. The substrate was transferred from the preparation chamber to the growth chamber by a manipulator. The growth chamber was isolated from the preparation chamber by a gate valve and was evacuated to 7×10^{-11} Torr by an ion pump and a titanium sublimation pump. The load-lock facilitates the introduction and removal of samples without significantly influencing the growth chamber vacuum. Liquid nitrogen shrouds equipped in the growth chamber were helpful in maintaining an ultra-high vacuum. Here nude gauges were used to measure the chamber base pressure. In addition, specific background gas species were monitored by a quadrupole mass analyzer. The growth temperature of superlattices could be changed from 20 to 1,000 K by the cooling and heating systems. The substrate temperature was monitored by the AuFe-chromel or chromel-alumel thermocouples in direct contact with the gold-coated substrate holder. The component metals of the superlattices were deposited using individual Knudsen cells. They consisted of a heating element, surrounding heat shield, and crucible thermocouple assembly mounted on a port flange. Source evaporants were contained inside PBN crucibles which fit into the furnace assembly. The pneumatically controlled shutters of the Knudsen cells were controlled on-line by a computer system (NEC PC-9801 VM) interfaced with an oscillating quartz thickness sensor (ULVAC CRTM-3) calibrated by a TALYSTEP (Rank Taylor Hobson). A typical preparation program was as follows; metal A was deposited for a Å, followed by an intermission of 5 sec, then metal B was deposited for b Å, and the process was repeated.

2. Structural Analysis

2.1 Reflection high-energy electron diffraction (RHEED)

A schematic diagram of a RHEED experiment (EIKO MB-1000) equipped in the MBE apparatus is shown in Figure 2. The electron gun, G, is similar to that used in conventional electron microscopes except that the vacuum seal part is specially made of glass. Both the diameter of slit SL_2 and the diameter of the direct spot on the fluorescent screen SC are 0.1 mm, resulting in a beam divergence of about $1x10^{-4}$ rad. The electron beam from G passes through SL_2

, converges by means of a

magnetic lens L, impinges upon sample S, and produces very bright and sharp diffraction patterns on SC. The RHEED patterns observed from V were photographed by an instant camera. The acceleration voltage used was 30 kV. The incident electron beam angle was about 1 degree relative to the sample surface.

2.2 X-ray diffraction (XRD)

Small-angle XRD is a very powerful and nondestructive method for determining how regular the alternately-deposited layers are stacked and how sharply the interfaces are formed. If the lattice spacing is d, diffraction peaks will be observed at angles θ satisfying the well-known Bragg equation:

$$2d\sin\theta = n\lambda_X,$$

where λ_X is the x-ray wavelength. Since the period of artificial compositional modulation is usually much longer than the lattice spacings in natural crystals, the peaks are observed in the small-angle region. In the present study, the superperiodicities of synthesized samples were determined from the observed lowest-order diffraction using the Bragg equation.

To obtain information on the crystal structure of individual layers in the superlattices, peaks in the middle-angle region have to be studied. For epitaxial superlattices, sharp peaks with satellites are observed. In the present study, x-ray diffraction simulation using a statistical model proposed by Mikolajczak et al.[1] was employed in order to provide further insight into the structural characteristics of epitaxial superlattices. The concept behind this model is that a large number of textured grains with different thicknesses are present in the growth direction of superlattice as shown in Figure 3. When this occurs, XRD intensity can be described by the following equation:

$$I(\theta)=L(\theta)\Sigma_{1}^{N}[\Sigma_{1}^{T_l}\Sigma_{j=1}^{T_l(m+n)} f_{l,j}(\theta)D_{l,j}W_{l,j}\exp(\frac{i4\pi x_{l,j}\sin\theta}{\lambda\chi})]^2,$$

where $L(\theta)$ consists of the polarization, Lorentz, and geometric factors:

$$L(\theta)=\frac{1+\cos(2\theta)}{\sin\theta\sin(2\theta)}$$

and N is the number of columns used in the calculations. T_l is the thickness of the lth grain expressed as the number of "unit cells". Here the "unit cell" means one period of superlattice. The variables m and n are the thicknesses of component metals as described by the number of monolayers. $f_{l,j}(\theta)$ are the averaged atomic scattering factors:

$$f_{l,j}(\theta)=C^A_{l,j}f^A(\theta)+C^B_{l,j}f^B(\theta)$$

$C^A_{l,j}$ and $C^B_{l,j}$ are the concentrations of A and B elements in the jth plane of the lth grain, and $f^A(\theta)$ and $f^B(\theta)$ are the atomic scattering factors for A and B, respectively. $D_{l,j}$ and $W_{l,j}$ are the averaged density of atoms in the jth plane and the averaged Debye-Waller coefficients, respectively, calculated in the same way as the factor $f_{l,j}(\theta)$. In this study, the Debye-Waller coefficients of rare-earth elements were estimated from their Debye temperatures.[2] The coordinates of the jth plane are

$$x_{l,j}=x_{l,j-1}+C^A_{l,j}d_A+C^B_{l,j}d_B,$$

where d_A and d_B are the interplanar distances for bulk A and B metals. In the comparison between the experimental and calculated XRD data, there are three important factors. They are the peak position, halfwidths of the peak, and peak intensity. In the first step of simulation, the thicknesses of component metals in the unit cell of superlattice, m and n, were determined by assuming an ideal superlattice structure without interdiffusion and texturised grains. Here only the peak position in the XRD pattern is strongly influenced by the values of m and n. Next, the structural coherence length can be estimated from the value of T_l. This parameter strongly contributes to only the halfwidths of the XRD peak. The concentration modulation at the superlattice interface can be found from the values of $C^A{}_{l,j}$ and $C^B{}_{l,j}$. Here small change in these parameters induces a large change in the intensity ratio between the main and satellite peaks. The values of m, n, T_l, $C^A{}_{l,j}$, and $C^B{}_{l,j}$ were determined by a Monte Carlo method.

In the present study, the small- and middle-angle XRD patterns of the samples were measured with a Rigaku CN2013 diffractometer using CuKα radiation.

2.3 Transmission electron diffraction (TED)

In the present study, TED patterns were measured using a transmission electron microscope (Akashi EM-002A) with a 120 keV electron beam. The samples for the TED observation were prepared by dissolving away the NaCl substrate in pure water.

3. Elemental Analysis

3.1 Electron probe micro analysis (EPMA)

In the present study, a Tracor Northern TN5500 electron probe micro analyzer attached to a scanning electron microscope (JEOL JSM-T330) was used to check impurity levels.

3.2 Auger electron spectroscopy (AES)

In the present study, PERKIN ELMER SAM 660, PHI 4300, or JEOL JAMP-10S spectrometers were used for elemental analysis. The depth profile using ion mill AES was measured by a PHI 4300 spectrometer. Sputter etching was done with a 1 keV Ar^+ ion beam at an incident ion-beam angle of 20 degrees relative to the sample surface, the ion current and etching area being 500 nA and 2x2 mm^2, respectively.

4. Magnetic Analysis

The DC magnetization was measured using a superconducting quantum interference device (SQUID: Hoxan HSM-2000). The measurement temperature range was between 4.2 and 200 K. The temperature change was controlled at a rate of 1 K/min. Samples were placed parallel to the external applied magnetic-field to measure the parallel magnetization ($M_{//}$). An applied static magnetic-field of up to 5,000 G was used.

References

[1] M. Jalochowsi and P. Mikolajczak, J. Phys. F 13, 1973 (1983).

[2] L. J. Sundstrom, in Handbook of the Physics and Chemistry of the Rare Earths, edited by K. A. Gschneidner, Jr. and L. Eyring (North-Holland, Amsterdam, 1978), Vol. 1, p. 379-410.

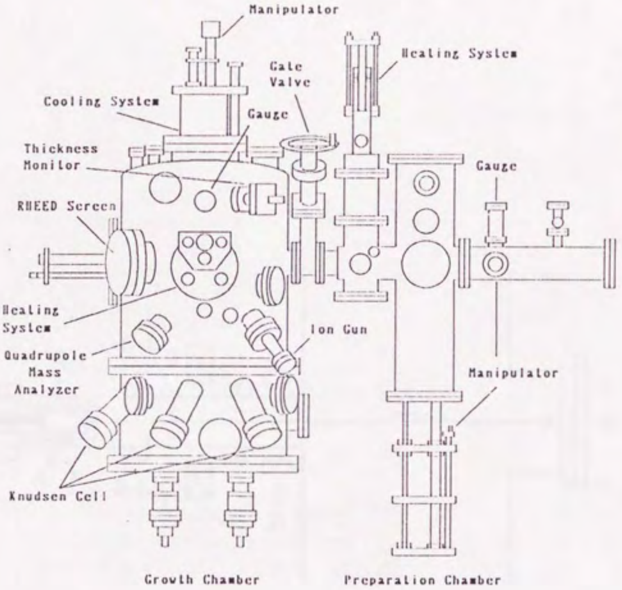

Figure 1. Schematic diagram of MBE apparatus.

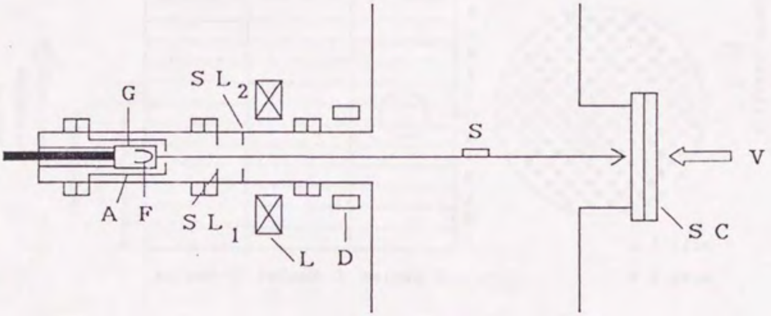

Figure 2. Schematic experimental arrangement for RHEED analysis. G: electron gun, F: filament, A: anode, SL_1: first slit, SL_2: second slit, L: magnetic lens, D: beam deflector, S: sample, and SC: fluorescent screen.

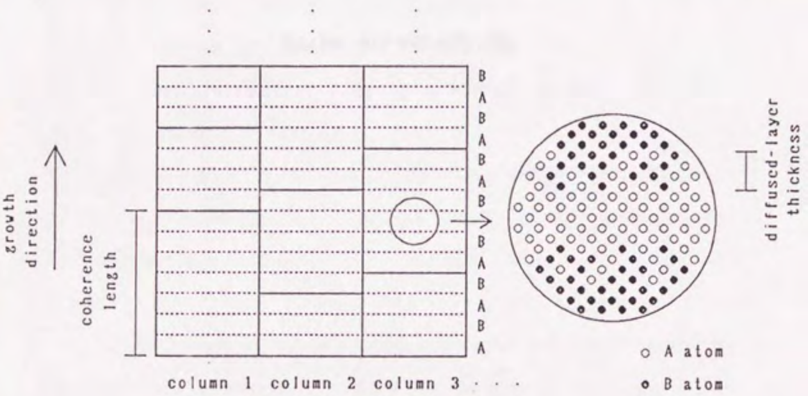

Figure 3. Model of non-ideal superlattice structure.

CHAPTER III

Eu/Mn SUPERLATTICE

1. Introduction

Binary phase diagrams can be classified into four categories:

- (A) two elements form solid solution in wide compositional ranges;
- (B) mutual solubility is limited but some intermetallic compounds exist;
- (C) homogeneous mixing is only possible in the liquid state;
- (D) homogeneous mixing is impossible even in the liquid state.

The formation of metallic superlattices is possible not only for category A, but also for other categories.[1] For the physical properties, there is great interest in superlattices consisting of eutectic (category C) or insoluble (category D) combinations because they make possible entirely new materials possessing superlattice structures. This is because bulk alloys cannot be formed in either system. From this point of view, Eu and Mn metals which are mutually insoluble[2] were selected as the components for the metallic superlattice discussed in this chapter. The mutual insolubility of Eu and Mn metals is expected to be effective for the elimination of interdiffusion between successive layers in the superlattices.

For Eu metal, neutron diffraction measurements have clearly demonstrated the first-order character of the magnetic transition. In the antiferromagnetic state below T_N=90.5 K, the moments form a spiral structure described by a wave vector along the [100] direction, such that the interplanar turn angle is close to 50 degrees.[3] On the other hand, Mn metal is known to have four solid phases, α , β , γ , and δ , below its melting point. The α -Mn phase which is stable under ambient temperature and pressure is found to be antiferromagnetic below 95 K.[4] Thus, because Eu and Mn metals possess magnetic spins, superlattice materials comprising both metals should be promising systems for investigating magnetic characteristics derived from interfacial exchange coupling between the Eu and Mn layers.

In the present work, superlattices composed of alternating layers of Eu and Mn metals were fabricated by means of the MBE technique. Reported here are the results from analysis of the structures and magnetic properties of the prepared Eu/Mn superlattices by RHEED, XRD, AES, and SQUID.

2. Experimental

Si (100) wafer whose typical size was 30x15x0.3 mm^3, except when otherwise indicated, was used as the substrate. Since the Eu metal readily makes a silicide, the Si surface was terminated with hydrogen using the Takahagi et al.'s method[5] after chemical etching. Eu (99.99 %) and Mn (99.999 %) metals were used as the source materials. Both metals were deposited at a rate of 0.2 Å/sec under ultra-high vacuum at 9×10^{-10} Torr using two Knudsen cells in an MBE apparatus. The growth temperature was kept between 260 and 295 K, except when otherwise indicated, in order to suppress interlayer diffusion. As the first step, an Eu layer was grown on a Si substrate. Following this, the Mn and Eu metals were alternately deposited. A 300 Å-thick Au layer was deposited on the surface of all finished samples in order to protect them from oxidation.

3. Structural Characteristics

3.1 Artificial superperiodicity

Figure 1 shows the XRD patterns in the small-angle region between 1 and 6 degrees obtained for Eu/Mn superlattices having different periodicities (Λ =19.0, 45.7, 77.3, 116, and 227 Å), in which the thickness of each layer are the same for Eu and Mn components, together with the data at higher angle region from 26 to 30 degrees. Sharp and intense (00L) reflection, accompanied by higher-order reflections, can be seen in the small-angle diffraction patterns. Note that even the specimen with an extremely small superlattice spacing, 19 Å, exhibits a sharp and intense basal reflection. The layer lattice spacing (Λ) described of each synthesized sample was determined from the lowest-order diffraction. Since the number of layers in each sample is known from the condition of preparation, it can be reconfirmed the spacing of the layer lattice by dividing the total thickness (D) of the film, measured by the quartz thickness monitor, with the periodicity number (N). The values of (D/N) thus obtained plotted against the layer lattice spacing determined from x-ray diffraction (Figure 2) are in good agreement. This implies that the superlattice has been grown successfully with the formation of smooth and clear interfaces.

Figure 3 shows the result of AES depth profile of an Eu/Mn superlattice of Λ=77.3 Å with 50 periods. Alternating Eu and Mn peaks can be observed up to 12 periods from the top surface in spite of the ion mixing produced by the analysis process. This result also supports the regularity of the Eu/Mn superlattice structure. The profile shows that the thickness of the Eu layer is equal to that of the Mn layer as designed. The presence of oxygen in the top three layers is due to sample oxidation on exposure to air during sample transfer to the AES spectrometer. No other impurities were detected both by EPMA and by AES analyses as shown in Figures 4 (a) and (b).

3.2 Structures of individual layers

In the case of the samples with $\Lambda \leqq 45.7$ Å, the observed XRD pattern showed only a very broad peak in the middle-angle region of Figure 1, indicating that both the Eu and Mn layers are in the amorphous state. However, the diffraction peak becomes narrower as the layer spacing increases, and a sharp crystalline diffraction peak corresponding to Eu (110) was observed in the diffraction pattern of the sample with a layer spacing of 227 Å. Here note that Eu layer took [110]-oriented crystalline structure even when the deposition temperature was as low as about 290 K, whereas Mn layer was amorphous irrespective of its thickness at the same deposition temperature. This finding raised a question why and how a thin Eu layer took a single-crystal-like structure. The XRD patterns of Eu thin films deposited on various substrates are shown in Figure 5. A sharp and intense diffraction peak due to Eu (110) plane was observed on all samples, together with a small diffraction peak attributable to Eu (220). From the comparison with the peak width of the diffraction from sapphire single-crystal substrate, the crystallinity of the deposited Eu film was concluded to be extremely good. The Eu (110) interplanar distance was determined to be

3.246± 0.002 Å using the XRD data obtained on a number of different Eu films. This lattice constant agrees, within experimental error, with the corresponding value 3.24 Å reported for bulk Eu metal. The orientation of (110) plane observed here cannot be due to the specific interaction with the substrate, because the Eu thin films deposited on different substrates including amorphous Mn (a-Mn) exhibited the same preferred orientation. Therefore, this is likely to be due to that the (110) plane is the most densely close-packed plane in the bcc-Eu crystal.

In addition, in-situ RHEED was observed during the deposition in order to provide further insight into the structural aspect of individual Eu or Mn layer. Figure 6 shows the change of RHEED patterns during Eu deposition on Si (100) at 251 K. The 1x1 pattern of the hydrogen-terminated Si surface disappeared as soon as the Eu metal was deposited. Then dim spots appeared overlapping the halo pattern when the thickness of the Eu layer approached 25 Å. These dim spots became intense and the halo pattern disappeared as the thickness of Eu layer increased. No further variation of the RHEED pattern was observed on increasing the thickness above 100 Å. The change of RHEED pattern during deposition was almost the same when Eu was deposited on other substrates. The spotty RHEED pattern observed here indicates the presence of randomly-oriented domains in the Eu (110) plane as assigned in Figure 7. Here any expansion and contraction of Eu lattice were not observed in the quantitative analysis of RHEED pattern. On the other hand, the RHEED study showed that Mn layer remained amorphous irrespective of the thickness. These RHEED observations are good agreement with results of XRD analysis. To summarize the observations mentioned above, it is suggested that the structure of the Eu/Mn superlattice is as follows. A-Mn and amorphous Eu (a-Eu) are alternately stacked in the samples with $\Lambda \leqq 45.7$ Å. On the other hand, a crystalline Eu layer (c-Eu) with a textured structure is present between an a-Eu layer and an a-Mn layer in the samples with $\Lambda \geqq 77.3$ Å. In this case, the thickness of the a-Eu layer is likely to be 25 Å, and that of the c-Eu and a-Mn layers are $\Lambda/2-25$ and $\Lambda/2$ Å, respectively. Such an unique structure in which the crystalline component gradually grows on the amorphous component with increasing its thickness has been often seen in the superlattices composed of rare-earth and transition metals, for example Dy-Fe[6] and Nd-Fe[7] systems.

4. Magnetic Characteristics

4.1 Thermal hysteresis phenomena

Figure 8 shows the temperature dependence of the parallel magnetization for Eu/Mn superlattices with various periodicities which was measured in the heating process under a magnetic field of 1,000 G. The magnetization for field-cooled and zero-field-cooled samples are described by the solid and broken lines, respectively. In these samples, the thickness of each layer are the same for both components and the total thickness to be about 4,000 Å (thus, the period ranged from 25 to 200 times). A strong thermal hysteresis resulting from different cooling conditions was observed in the samples with $\Lambda \leqq 45.7$ Å. Namely, a remarkable increase of magnetization was observed in the samples which were cooled from ambient temperature to 4.2 K under 1,000 G. The zero-field-cooled samples were in the magnetic-frozen state, characterized by a clear cusp, at low temperature. On the other hand, such a thermal hysteresis was not observed in samples with Λ larger than 77.3 Å. Figure 9 shows the temperature dependence of the parallel magnetizations measured for the Eu/Mn superlattices, in which the Eu layer thickness is held constant at 20 Å and the thickness of the intervening Mn layers are varied form 20 to 50 Å. The cusps observed are found to become broad with increasing of the Eu interlayer distance (equivalent to the Mn layer thickness). In addition, the thermal hysteresis, which is estimated by the difference between the magnetizations of field-cooled ($M_{F//}$) and zero-field-cooled ($M_{Z//}$) samples at 4.2 K, becomes smaller as the Eu interlayer distance increases, as shown in Figure 10. As a result, the thermal hysteresis and cusp were not clearly detected in the Eu/Mn superlattices with Eu interlayer distances greater than 70 Å. Here the Mn layers themselves are not likely to play a role in the observed magnetism because the magnetization decreased with increasing Mn layer thickness. Since the superlattices prepared possess the same Eu layer thickness and same periodicity number (= 25), all samples are equivalent as far as the contribution from each Eu layer. This finding leads to the speculation that the individual Eu layers in superlattices can be magnetically coupled to each other and the unique magnetism observed here is mainly associated with the Eu interlayer interaction not the interfacial interaction between Eu and Mn layers. This can be supported by the experimental result that such unique magnetic behavior was not observed in the Eu/Mn superlattices with long periods (see Figure 8), in spite of the presence of a Eu-Mn interface. That is, a long-range magnetic interaction between the Eu layers becomes weaker as the thickness of the "spacer", such as the Mn layers, is increased. The origin of the Eu interlayer interaction could be due to the long-range RKKY interaction since the RKKY interaction between the 4f spins, which is mediated indirectly through the polarization wave in the conduction bands, is known to contribute significantly to the magnetism of the Eu metal.

4.2 Magnetic anisotropy

Typical magnetization curves obtained at 4.2 K for Eu/Mn superlattices are shown in Figure 11. The field-cooled sample was initially cooled from ambient temperature to 4.2 K under 5,000 G. The observation of saturated and residual magnetization suggests the presence of ferromagnetic components. No elements that can act as ferromagnetic impurities were detected by EPMA and AES measurements, as shown in Figures 4 (a) and (b). Therefore, the appearance of ferromagnetism here is due to the superlattice structure, since Eu[3] and Mn[4] are antiferromagnetic in their bulk states. The hysteresis loops obtained for the zero-field-cooled Eu/Mn superlattices were symmetrical. In contrast, anti-symmetrical hysteresis loops were observed for the field-cooled superlattices. This indicates that unidirectional anisotropy exists in this system. The unidirectional anisotropy generally arises under the coexistence of ferromagnetism and antiferromagnetism.[8] The sign of the RKKY interaction alternates with the change in the distance between the magnetic spins and the RKKY interaction can lead to ferromagnetic or antiferromagnetic ordering depending on electron lattice and moment parameters.[9] Therefore, the unidirectional anisotropy in the Eu/Mn superlattices is likely to be due to the long-range interlayer interaction which contributes to the thermal hysteresis phenomena.

4.3 Magnetic-frozen states

Figure 12 shows a typical temperature dependence of the parallel magnetization for Eu/Mn superlattices with atomic-scale periodicities measured under 10 G. It is worth noting that three cusps were clearly observed for the zero-field-cooled superlattices. Since a thermal hysteresis is observed for cusp C_1 with the highest frozen temperature, the magnetic-frozen transition occurs exactly at C_1. Up until now, two cusps have been known in re-entrant spin-glass materials. However, thermal hysteresis is observed at the lower temperature cusp in re-entrant spin-glass materials because the cusp with higher temperature corresponds to an antiferromagnetic ordering.[10] Therefore, the presence of multiple cusps in the Eu/Mn superlattices can't be explained by the re-entrant spin-glass behavior and is likely to be a new magnetic phenomenon. One possible model for multiple cusps is that some metastable states associated with domain structure exist in the magnetic-frozen phase. The different barrier energy which is necessary for the spin-inversion in each domain introduces a few relaxation process to frozen behavior. Moreover, the distribution of barrier energy is sensitive against the temperature.[11] Figures 13 (A) and (B) show the temperature dependence of the parallel magnetizations obtained under various magnetic-fields for a zero-field-cooled Eu (30 Å)/Mn (20 Å) superlattice with 25 periods. It is interesting that the number of cusps and frozen temperature which is defined by the position of the cusps gradually change with increasing magnetic-field. The C_1 cusp gradually broadened and its frozen temperature fell as the magnetic-field increased from 10 to 200 G. Correspondingly, the second cusp (C_2) became the dominant cusp over the same magnetic-field range. Under magnetic-fields between 200 and 1,000 G, the C_2 cusp possessed the same magnetic-field dependence as the C_1 cusp. The C_3 cusp with the lowest frozen temperature changed little with increasing magnetic-field from 10 to 1,000 G. In the magnetic-frozen states reported to date as spin-glass, the magnetic-field dependence has been evident as a broadening of the cusp,[12] where the frozen temperature changes little during measurement under static magnetic-fields.[13] Therefore, the magnetic-field dependence observed for Eu/Mn superlattices is the first case.

References

[1] T. Shinjö, in Metallic Superlattices, edited by T. Shinjo and T. Takada (Elsevier, Amsterdam, 1987), p. 1-32.

[2] P. Villars, J. Less-Common Met., 110, 11 (1985).

[3] A. H. Millhouse and K. A. McEwen, Solid State Commun., 13, 339 (1973).

[4] T. Yamada, J. Phys. Soc. Jpn., 28, 596 (1970).

[5] T. Takahagi, I. Nagai, A. Ishitani, H. Kuroda and Y. Nagasawa, J. Appl. Phys., 64, 3516 (1988).

[6] K. Yoden, N. Hosoito, K. Kawaguchi, K. Mibu and T. Shinjo, Jpn. J. Appl. Phys., 27, 1680 (1988).

[7] K. Mibu, N. Hosoito and T. Shinjo, J. Phys. Soc. Jpn., 58, 2916 (1989).

[8] J. S. Kouvel and C. D. Graham, Jr., J. Appl. Phys., 30, 312S (1959).

[9] M. Ruderman and C. Kittel, Phys. Rev., 96, 99 (1954); T. Kasuya, Prog. Theor. Phys., 16, 45 (1956); K. Yosida, Phys. Rev., 106, 893 (1957).

[10] A. Ito, H. Aruga, M. Kikuchi, Y. Syono and H. Takei, Solid State Commun., 66, 475 (1988).

[11] K. Nemoto and H. Takayama, J. Phys. C 16, 6835 (1983).

[12] V. Cannella and J. A. Mydosh, Phys. Rev. B 6, 4220 (1972).

[13] B. Barbara, A. P. Malozemoff and Y. Imry, Physica B 108, 1289 (1981).

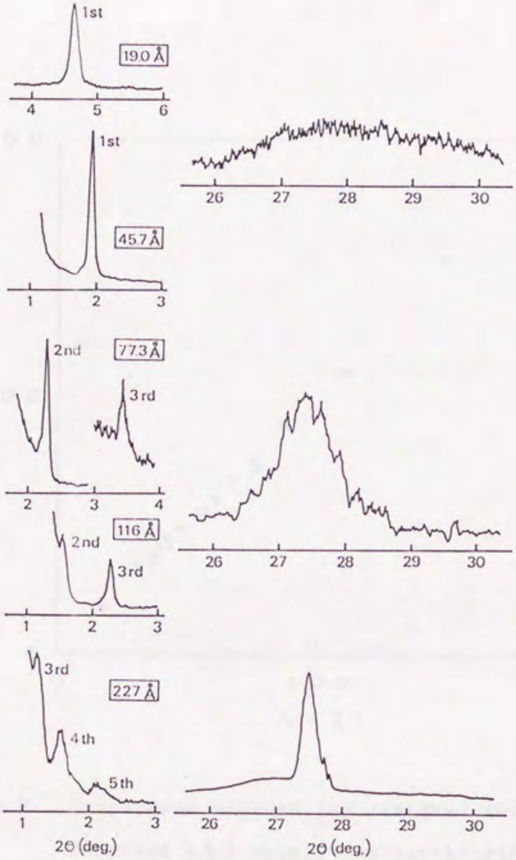

Figure 1. Small- and middle-angle XRD patterns for Eu/Mn superlattices having different periods.

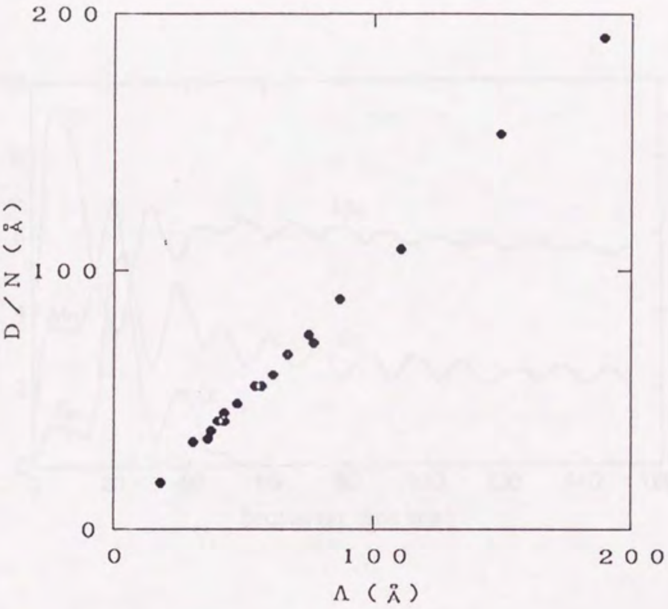

Figure 2. Comparison between the designed (D/N) and observed (Λ) modulation wavelengths in Eu/Mn superlattices.

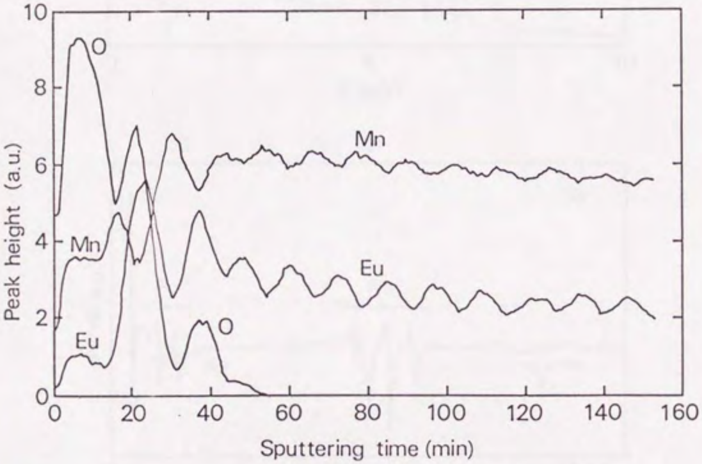

Figure 3. AES depth profile of Eu/Mn superlattice with Λ =77.3 Å and 50 periods.

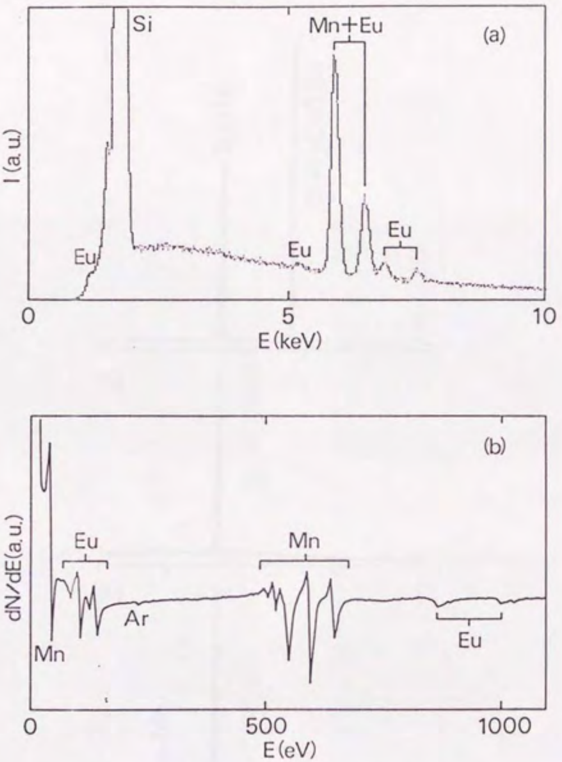

Figure 4. Typical (a) EPMA and (b) AES spectra of Eu/Mn superlattices.

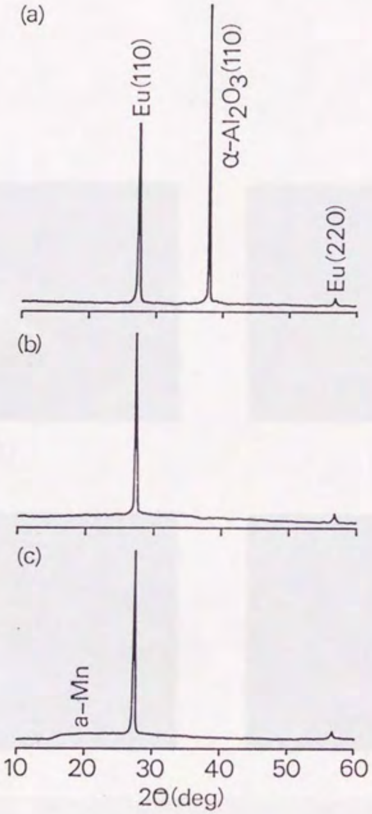

Figure 5. XRD patterns of Eu thin films deposited on various substrates. (a) on sapphire $(11\bar{2}0)$ at 260-266 K, (b) on Si (100) at 274-277 K, and (c) on amorphous Mn at 268-273 K.

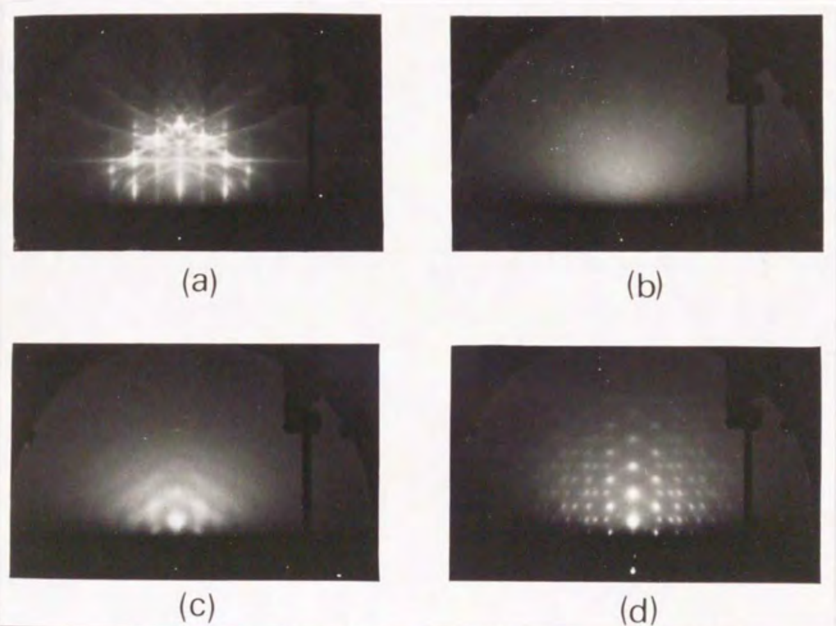

Figure 6. Change of in-situ RHEED patterns for Eu thin film deposited on Si (100) at 251 K. (a) 1x1 hydrogen-terminated Si surface, (b) 15 Å-thick Eu film, (c) 25 Å-thick Eu film, and (d) 100 Å-thick Eu film.

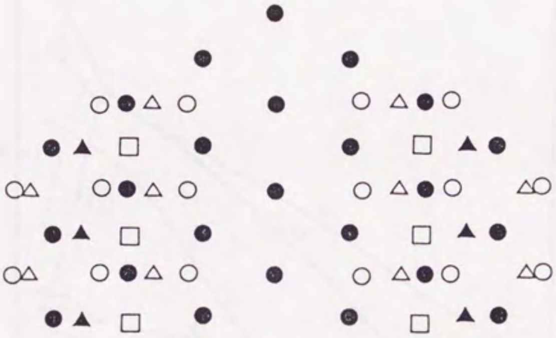

Figure 7. Calculated RHEED patterns for Eu (110) ([111]: ●, [100]: ○, [110]: △, [311]: □, and [133]: ▲).

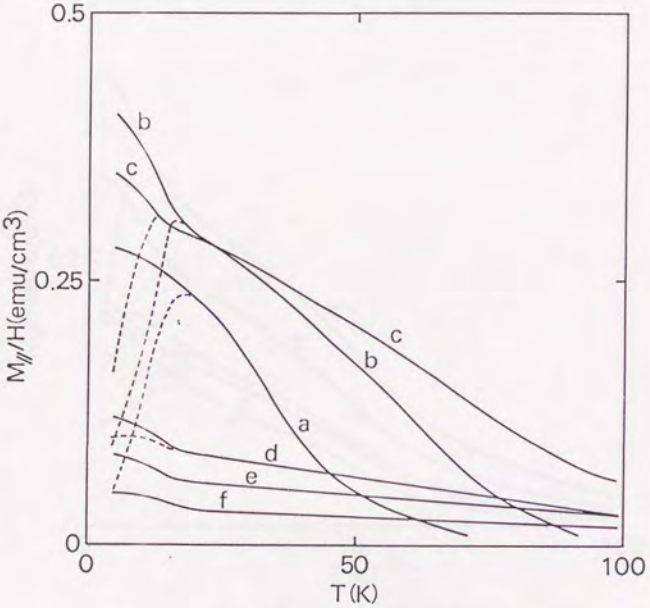

Figure 8. Temperature dependence of parallel magnetizations for Eu/Mn superlattices having different periods (a: 19.0, b: 30.6, c: 45.7, d: 77.3, e: 116, and f: 155 Å). Solid and broken lines were measured for field-cooled and zero-field-cooled samples, respectively, under 1,000 G.

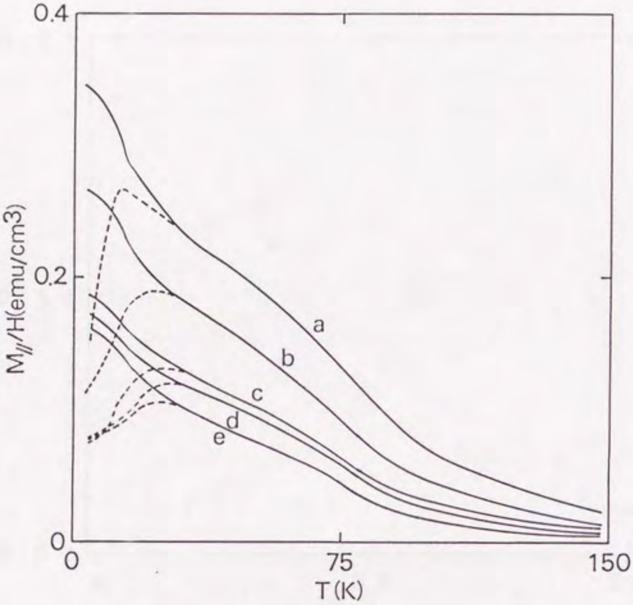

Figure 9. Temperature dependence of parallel magnetizations for Eu (20 Å)/Mn superlattices with various Eu interlayer distances (a: 19.6, b: 28.8, c: 35.2, d: 40.9, and e: 50.1 Å) as measured in a magnetic field of 1,000 G for field-cooled (solid line) and zero-field-cooled (broken line) samples.

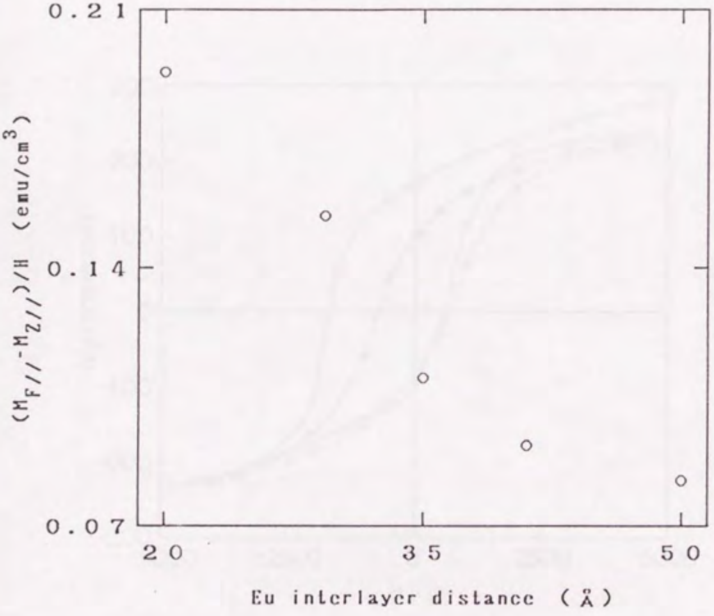

Figure 10. Thermal hysteresis at 4.2 K under 1,000 G versus Eu interlayer distance for Eu (20 Å)/Mn superlattices.

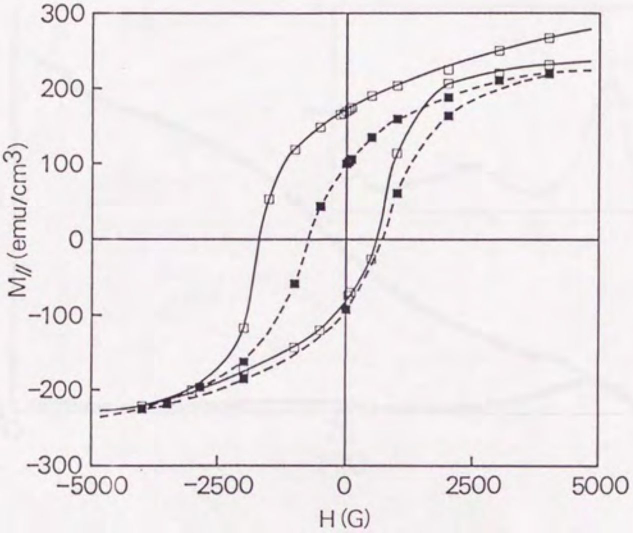

Figure 11. Parallel magnetization curves at 4.2 K for field-cooled (□) and zero-field-cooled (■) Eu (20 Å)/Mn (50 Å) superlattice with 25 periods.

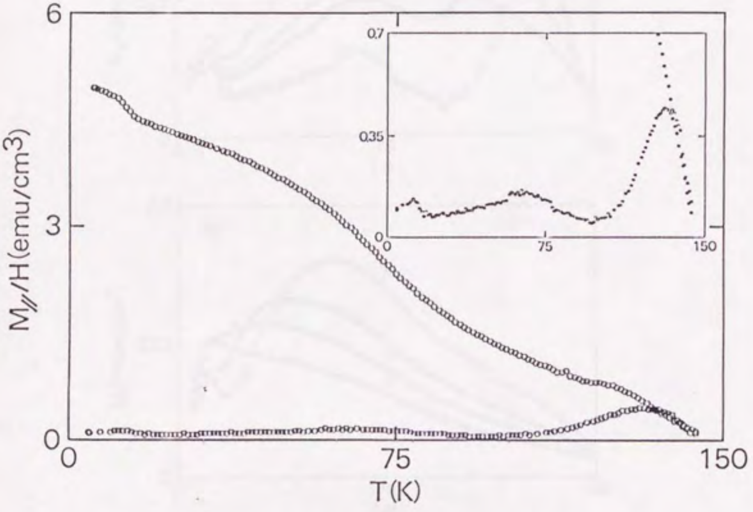

Figure 12. Temperature dependence of parallel magnetizations for field-cooled and zero-field-cooled Eu (30 Å)/Mn (20 Å) superlattices with 25 periods as measured in 10 G. The insert expands the magnetic data for the zero-field-cooled sample.

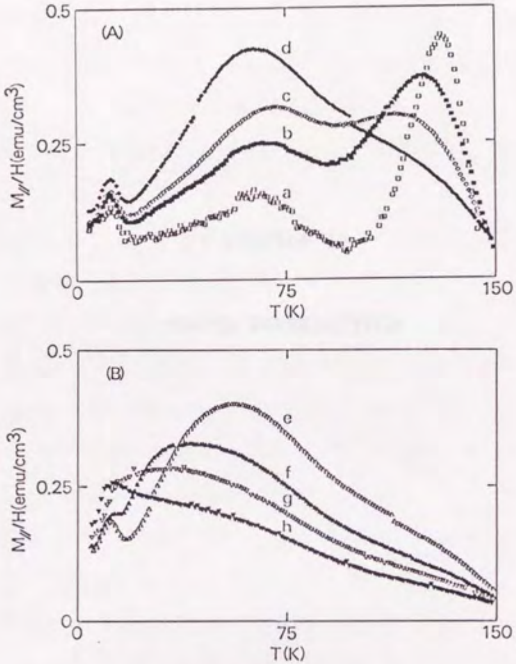

Figure 13. Temperature dependence of parallel magnetizations for zero-field-cooled Eu (30 Å)/Mn (20 Å) superlattice with 25 periods as measured in various magnetic-fields. The magnetic-fields (G) are a: 10, b: 50, c: 100, and d: 200 in figure (A) and e: 300, f: 500, g: 700, and h: 1,000 in figure (B).

CHAPTER IV

Eu/Yb SUPERLATTICE

1. Introduction

Under ambient pressure, Yb metal possesses the fcc structure (a=5.481 Å) up to 1,071 K, above which it changes to the bcc structure (a=4.44 Å).[1] On the other hand, the bcc structure (a=4.578 Å) of Eu metal is stable up to the melting point, 1,095 K, under ambient pressure.[1] Here the lattice constant of the high-temperature bcc phase of Yb metal is very close to that of the bcc-Eu phase, the lattice mismatch between the bcc phases of these two metals being only 3.01 %. Therefore, it is highly promising that the bcc-Yb phase can be obtained when a thin Yb layer is epitaxially grown on a bcc-Eu metal layer. It may also be possible to prepare a superlattice system consisting of bcc-Eu and bcc-Yb layers.

Neutron diffraction studies on a single crystal sample of Eu metal have indicated that it possesses a first-order transition to an antiferromagnetic state corresponding to a spiral structure along a cube axis at 90.5 K.[2] The turn angle per layer was observed to vary only slightly from 51.4 degrees at T_N to 50.0 degrees at 4.2 K. It is well known that the RKKY interaction between the 4f spins, which is mediated indirectly through the polarization wave in the conduction bands, contributes significantly to this complex magnetic structure of the Eu metal. On the other hand, Yb metal is essentially non-magnetic because the 4f orbital is occupied. Therefore, superlattice materials comprising both metals would seem to be promising systems for investigating the modulation effects derived from long-range interlayer exchange coupling. Because the modulation effects can be readily explored by simply varying the intervening non-magnetic Yb layer thickness while maintaining a constant magnetic Eu layer thickness. In addition, the superlattices, in which the Yb layer is thick enough that the interaction between Eu layers is negligible, can be considered as a pseudo two-dimensional magnetic systems.

From these structural and magnetic points of view, the Eu/Yb superlattices with various periods were investigated. Reported here are the formation of Eu/Yb superlattices using the MBE method and the structural and magnetic properties of the superlattices which were elucidated by RHEED, XRD, and SQUID.

2. Experimental

An NaCl single crystal, typical size 30x15x3 mm^3, was used as the substrate. The NaCl crystals were introduced to the preparation chamber as soon as their (100) planes were cleaved under ambient atmosphere. Eu (99.99 %) and Yb (99.99 %) metals were used as the source materials. Both metals were deposited at a rate of 0.2 Å/sec under ultra-high vacuum at 6×10^{-10} Torr using two Knudsen cells in an MBE apparatus. The growth temperature was kept at 260 K in order to suppress interlayer diffusion. As the first step, a 250 Å-thick Eu buffer layer was grown on a NaCl substrate having a cleaved (100) surface. Following this, the alternately deposition of the Yb and Eu metals was repeated 25 times for each sample. A 200 Å-thick Au layer was deposited on the surface of all finished samples in order to protect them from oxidation.

3. Structural Characteristics

3.1 Epitaxial growth of Eu buffer layers

Figure 1 (a) shows a typical RHEED pattern of a cleaved (100) surface of the NaCl crystal observed with the [100] incident azimuth. The observed RHEED pattern indicated that a clean (100) surface with a macroscopic step structure was formed by cleavage of the NaCl single crystal. Since NaCl is an insulator, the observed diffraction spots are rather dim due to the charged-up phenomenon. Eu was first deposited onto this NaCl (100) surface to form a buffer layer for the preparation of the Eu/Yb superlattice. The RHEED pattern of a 250 Å-thick Eu layer, observed for the same azimuthal angle as that of Figure 1 (a), is shown in Figure 1 (b). Two kinds of spots and/or streaks arising from the Eu (110) [100] and [110] coexist in this pattern. On the other hand, when the same sample was rotated around the axis normal to the sample surface, the RHEED pattern shown in Figure 1 (c) was observed, which can be attributed to Eu (110) [111]. This type of RHEED pattern appeared twice as the sample was rotated by 90 degrees from the orientation, which gave the RHEED pattern shown in Figure 1 (b). These experimental results indicate that the epitaxially grown Eu layer has a double-domain structure illustrated in Figure 2, orienting the Eu (110) plane parallel to the substrate. Namely, there is the epitaxial relationship that either Eu (110) [100] or [110] is parallel to NaCl (100) [100]. The existence of such an epitaxial relationship between the Eu layer and NaCl substrate was rather unexpected because the two-dimensional lattice unit in the Eu (110) plane is quite different from that in the NaCl (100) plane, as shown in Figure 3. However, it is worthy to note that the area of the two-dimensional unit cell in the Eu (110) plane is almost the same as that in the NaCl (100) plane, and furthermore, if the domain composed of 5x7 unit cells is considered in the Eu (110) plane, it matches well with the domain composed of 4x8 unit cells in the NaCl (100) plane. Seemingly, it is the geometrical relationship between the Eu (110) plane and the NaCl (100) plane that results in the epitaxial growth of the Eu layer with the double-domain structure illustrated in Figure 2.

3.2 Epitaxial growth of bcc-Eu/Yb superlattices

Eu/Yb superlattices with various periods were prepared over the 250 Å-thick Eu buffer layer. All the superlattice samples, in which the thickness of each layer are the same for Eu and Yb components, showed very sharp and intense diffraction peaks corresponding to their superlattice periodicities in their small-angle XRD patterns. The observed diffraction peaks are accompanied by the peaks due to the higher-order reflections as shown in Figure 4. The average superlattice periodicity should be D/N where D is the total thickness of the prepared superlattice and N the total number of the Eu (or Yb) layers. Using the D value measured with a quartz oscillating thickness monitor and the N value known from the condition of preparing a superlattice sample, the value of D/N was calculated and was plotted against the superlattice spacing Λ determined from XRD. There was a good agreement between D/N and Λ as shown in Figure 5.

Figure 6 (a) shows the middle-angle XRD pattern obtained for the Eu/Yb superlattice in which each layer of Eu and Yb is 32 Å-thick. Very sharp main peak observed at $2\theta=27.9$ degrees, which should correspond to the average (110) spacing in the superlattice, is located between those of the bcc-Eu (110) ($2\theta=27.5$ degrees) and bcc-Yb (110) ($2\theta=28.4$ degrees). Since the satellite peaks are clearly observed around this main peak, it is found that the structural coherence length in the Eu/Yb superlattice is greater than the superlattice periodicity. Here the x-ray diffraction simulation using a "statistical model (see Section 2.2 of Chapter II)" was carried out to obtain information on the structural parameters, such as interface diffusion and coherence length, of the superlattices. The values of the parameters in which the calculated spectrum was in agreement with the experimental spectrum suggested that the thickness of the inter-diffused layer and the structural coherence length were 4 atomic-layers and 9 "unit cells", respectively. The "unit cell" means one period of the superlattice. Here the RHEED pattern observed during Yb layer deposition showed the same symmetry as that of the Eu buffer layer grown on the cleaved NaCl substrate (see Figure 1), indicating a good epitaxial relationship between Yb and Eu lattices.

All the experimental results mentioned above show that epitaxial bcc-Eu/bcc-Yb superlattices, in which significant interdiffusion probably did not occur, were successfully grown on the Eu buffer layer formed on NaCl (100). It should be noted that the bcc structure of Yb is stable only above 1,071 K under ambient pressure in the case of the bulk Yb metal.[1] Nevertheless, Yb layers with the bcc structure corresponding to the high-temperature phase were formed in the Eu/Yb superlattice although the growth temperature was as low as 260 K. This means that the bcc structure of the Yb layer is formed and stabilized because of the epitaxial relationship with the bcc-Eu layer.

3.3 Epitaxial growth of bcc-Yb thick films

In order to examine the critical thickness of the epitaxial growth of the bcc-Yb layer, above which the structure of deposited Yb changes to the fcc ambient temperature phase, Yb was deposited up to the thickness of more than 1,500 Å on a 250 Å-thick bcc-Eu buffer layer epitaxially grown on NaCl (100). Figure 7 shows the XRD pattern of a 1,000 Å-thick Yb film thus prepared. In analyzing this diffraction pattern, it must be careful because the lattice spacings of bcc-Yb (110) (3.14 Å) and fcc-Yb (111) (3.165 Å) are nearly equivalent. However, the XRD measurement system used for this analysis possesses sufficient resolution to resolve the bcc-Yb (220) (2θ=58.8 degrees) and fcc-Yb (222) (2θ=58.27 degrees) lines as shown in the insert of figure 7. A sharp and intense diffraction peak due to the bcc-Yb (110) reflection was observed together with the diffraction peak attributable to the bcc-Yb (220) reflection. Peaks due to the [110]-oriented Eu buffer layer and that due to the NaCl substrate were also observed in the same diffraction pattern. Moreover, the RHEED patterns observed for the Yb films showed the same symmetry as those of the Eu buffer layer (bcc). Therefore, it is concluded that the Yb films prepared here possess a bcc structure. The diffraction peaks of the Yb layer were quite narrow, indicating extremely high crystallinity. The (110) spacing in the bcc-Yb layer was determined to be 3.135± 0.002 Å, taking the average over the values measured on a number of different samples prepared by the same procedures. This value is in agreement within experimental error with the reported spacing, 3.14 Å, of the bcc-Yb crystal which was prepared under high pressure.[1] The analysis of the RHEED pattern also showed that there is no expansion or contraction in the lattice of the Yb layer prepared in the present experiment. The Yb layer was found to remain entirely in the bcc phase up to a thickness of 1,500 Å. When the thickness of the Yb layer exceeded this value, the diffraction peaks due to the fcc phase appeared besides those due to the bcc phase, and the intensities of the former peaks increased with the thickness of the Yb layer, indicating the formation of the fcc-Yb phase over the bcc-Yb layer. From these results, it can be concluded that the Yb layer takes the bcc structure at least up to 1,500 Å when it is epitaxially grown on the bcc-Eu layer. Note that this critical thickness is large enough to be considered almost as a bulk state. The EPMA and AES measurements indicated that such a unique structural aspect of Yb metal was not due to the impurities as shown in Figures 8 (a), (b), and (c).

It has been generally considered impossible to fabricate a thick metal film having the structure which is stable in the bulk state only at a high temperature by utilizing the epitaxial relationship with the substrate. This is due to the fact that the stabilization effect by the epitaxial relationship should decrease on increasing the distance from the interface. In fact, the high-temperature fcc-Fe phase grown on the fcc-Cu substrate was reported to be stable only up to 15 atomic layers,[3] above which the structure of the Fe layer changed to the bcc phase, which is stable at the room temperature. In this respect, the Eu/Yb superlattice seems to be rather exceptional. Seemingly, there exists, by some reason, an especially strong epitaxial relationship between bcc-Eu and bcc-Yb layers. The fact that all samples prepared in the present study exhibited an extremely high crystallinity in the bcc-Yb layer, although the growth temperature was as low as 260 K, might also be related to the strong epitaxial interaction between Yb and Eu layers.

4. Magnetic Characteristics

4.1 Thermal hysteresis phenomena

The temperature dependence of the parallel magnetizations for epitaxial Eu/Yb superlattices with various Eu interlayer distances is shown in Figure 9. The Eu thickness of these samples was held constant at 20 Å. The magnetic data were obtained in a magnetic field of 50 G for field-cooled (under 50 G) and zero-field-cooled samples. Thermal hystereses resulting from different cooling conditions were observed for these samples. Namely, the field-cooled superlattices showed monotonic increase in the magnetization with decreasing temperature. In addition, the magnetic-frozen states, characterized by the cusp in the temperature dependent magnetization curves, were observed for the zero-field-cooled superlattices. It is worth noting that this unique magnetic behavior systematically changed with increasing thickness of the non-magnetic Yb layers. That is, the absolute values of magnetization gradually became smaller as the Yb thickness increased, even though the total volume of 4f magnetic spins are the same in all of the superlattices. The thermal hysteresis, which is estimated by the difference between the magnetizations of field-cooled ($M_{F//}$) and zero-field-cooled ($M_{Z//}$) samples at 4.2 K, also became smaller as the Eu interlayer distance increased, as shown in Figure 10. Moreover, the frozen temperature, as defined by the cusp position, decreased with increasing Eu interlayer distance as shown in Figure 10. As a result, the thermal hysteresis and cusp were not clearly detected in epitaxial Eu/Yb superlattices with Eu interlayer distances greater than 70 Å.

Based on the experimental results, it implies that the individual Eu layers in superlattices can be magnetically coupled to each other and the thermal hysteresis phenomena including the magnetic-frozen states observed are associated with the Eu interlayer interaction. Such a long-range interaction must be a RKKY-type interaction which is mediated by the 6s conduction electrons of Eu metal. Because the direct interaction between 4f spins which are localized in the inner core is negligibly small and is only effective over a short-range. The RKKY model yields an interaction which is oscillatory in character and can lead to ferromagnetic or antiferromagnetic ordering depending on electron lattice and moment parameters.[6] In the superlattices, the RKKY-type interaction is modulated by the superperiodicity. Therefore, the magnetic-frozen states are likely to be produced by an appropriate combination of ferromagnetic and antiferromagnetic interlayer interactions.

Next the epitaxial Eu/Yb superlattices with various Eu thickness were studied. Here the Yb thickness was fixed at 20 Å. As shown in Figure 11, thermal hystereses were also observed in the temperature dependence of the parallel magnetizations for these samples. However, the magnetic properties of this series did not systematically change with increasing Eu thickness. Namely, the absolute values of magnetization, the $M_{F//}-M_{Z//}$ values, and frozen temperature randomly changed against the increase of Eu thickness. This is probably due to a complex combination of factors which affect the interaction between the Eu layers in different ways. Such factors might include the pseudo two-dimensionality of the layers which become more bulk-like with increasing thickness.

4.2 Magnetic-field dependence

Figure 12 shows the temperature dependence of the parallel magnetizations measured under various magnetic-fields for the epitaxial Eu (40 Å)/Yb (20 Å) superlattice. The frozen temperature exponentially decreased as the magnetic-field became stronger, as shown in Figure 13. In addition, a critical magnetic-field was observed for the change in the thermal hysteresis, as shown in Figure 13. Namely, the thermal hysteresis increased until the magnetic-field reached 50 G, at which point it gradually decreased. Finally, the thermal hysteresis and cusp were not observed above 4.2 K under 300 G. This means that the Eu interlayer interaction which forms the thermal hysteresis possesses a strong magnetic-field dependence and is stopped when the magnetic-field reaches 300 G. In spin-glass materials, the magnetic-field dependence has been evident as a broadening of the cusp,[5] where the frozen temperature changes little during measurement under static magnetic fields.[6] In addition, though the Eu-Yb alloys have possessed the cusp corresponding to the antiferromagnetic transition in their temperature dependent magnetization curves, no magnetic-field dependence has been observed for the cusp position.[7] Therefore, unique magnetic-frozen behavior observed here are not due to the spin-glass or antiferromagnetic nature and they are inherent characteristics of the Eu/Yb superlattices.

4.3 Magnetic hysteresis

A typical magnetization curve obtained at 4.2 K for an epitaxial Eu/Yb superlattice is shown in Figure 14. The arrow indicates the starting point for the magnetic-field cycling on the sample which was cooled from ambient temperature to 4.2 K under 0 G. The observation of saturated and residual magnetization implies the presence of ferromagnetic components in the Eu/Yb superlattices. Here no elements that can act as ferromagnetic impurities were detected by EPMA and AES, as shown in Figures 8 (a), (b), and (c). In addition, the Eu-Yb alloys with high Eu concentration have been reported to be antiferromagnetic.[7] Therefore, the appearance of ferromagnetic behavior here is due to the superlattice structure since Eu and Yb are antiferromagnetic[2] and non-magnetic, respectively, in their bulk states. The extrapolated magnetization at 10,000 G was about 475 emu/cm^3 at 4.2 K. The magnetic moment of the Eu can be estimated to be 2.46 μ_B based on this value. Comparison with the theoretical saturated magnetic moment (7 μ_B) indicates that about 35 % of the Eu atoms are in a ferromagnetic state. Since such a big magnetic moment does not occur in the spin-glass state of diluted spin systems, the magnetic-frozen behavior observed is associated with the inherent nature of the superlattices as discussed above.

References

[1] B. J. Beaudry and K. A. Gschneidner, Jr., in Handbook of the Physics and Chemistry of the Rare Earths, edited by K. A. Gschneidner, Jr. and L. Eyring (North-Holland, Amsterdam, 1978), Vol. 1, p. 173-232.

[2] A. H. Millhouse and K. A. McEwen, Solid State Commun., 13, 339 (1973).

[3] M. Stampanoni, A. Vaterlaus, M. Aeschlimann, F. Meier and D. Pescia, J. Appl. Phys., 64, 5321 (1988).

[4] S. Tanuma, W. R. Datars, H. Doi and A. Dunsworth, Solid State Commun., 8, 1107 (1970).

[5] G. Johansen and A. R. Mackintosh, Solid State Commun., 8, 121 (1970).

[6] M. Ruderman and C. Kittel, Phys. Rev., 96, 99 (1954); T. Kasuya, Prog. Theor. Phys., 16, 45 (1956); K. Yosida, Phys. Rev., 106, 893 (1957).

[7] V. Cannella and J. A. Mydosh, Phys. Rev. B 6, 4220 (1972).

[8] B. Barbara, A. P. Malozemoff and Y. Imry, Physica B 108, 1289 (1981).

[9] S. Legvold and J. P. Beaver, Solid State Commun., 31, 727 (1979).

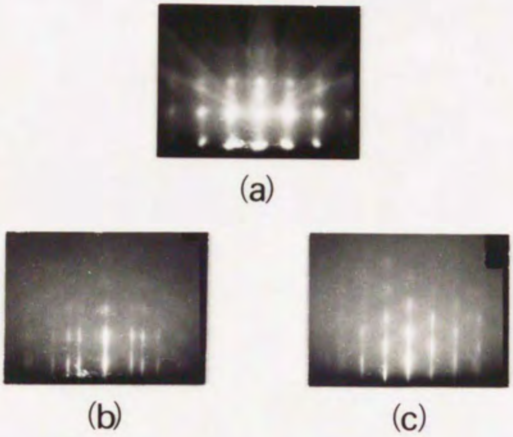

Figure 1. (a) RHEED pattern of the cleaved NaCl (100) surface observed with the incident azimuth of [100] and (b), (c) RHEED patterns of a 250 Å-thick Eu layer formed on NaCl (100). Pattern (b) is for the same orientation of the sample as (a) and can be assigned to Eu (110) [100] and [110]. Pattern (c) is for a different orientation and can be assigned to Eu (110) [111].

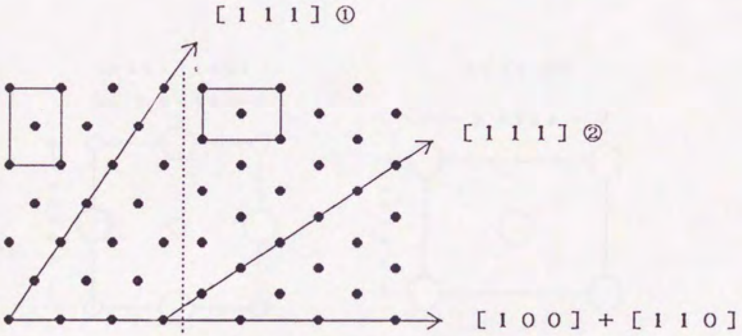

Figure 2. Illustration of the double-domain structure in the Eu buffer layer grown on NaCl (100).

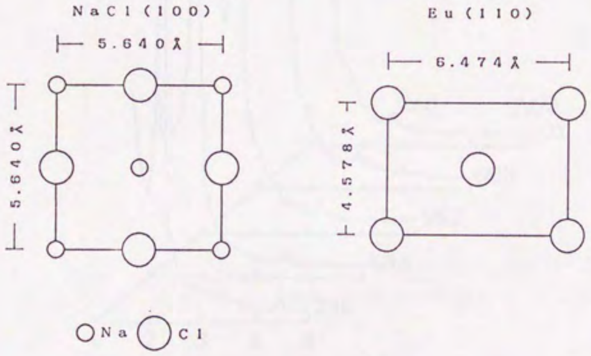

Figure 3. Two-dimensional lattice unit in the NaCl (100) plane and that in the Eu (110) plane.

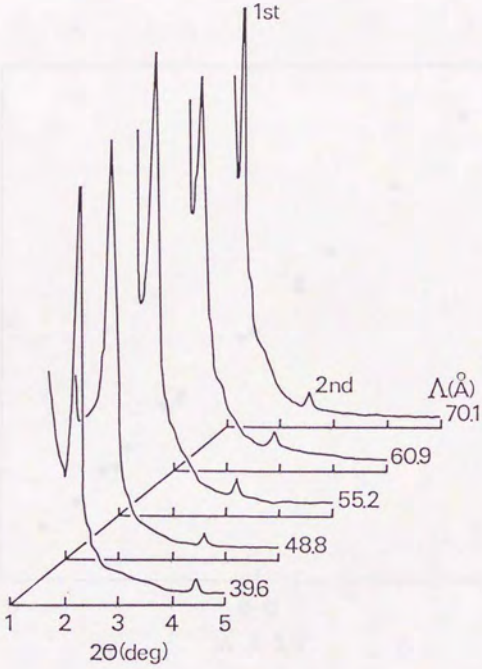

Figure 4. Small-angle XRD patterns of Eu/Yb superlattices with different superlattice periodicities.

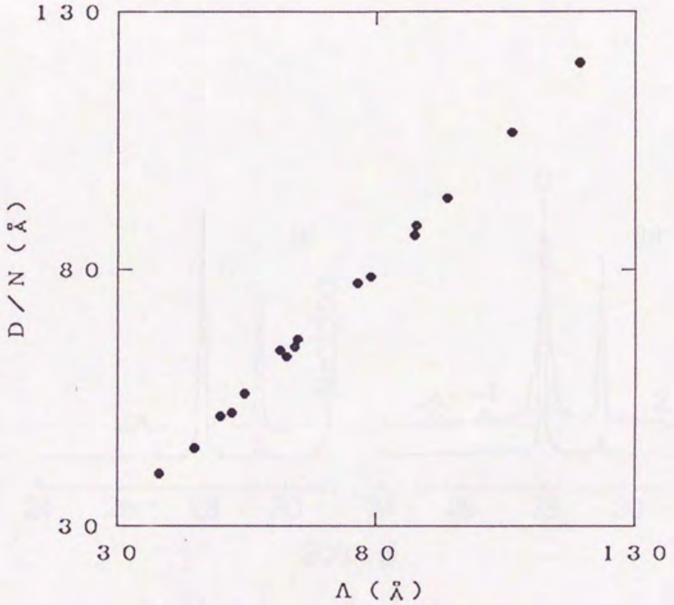

Figure 5. Comparison between the designed (D/N) and observed (Λ) modulation wavelengths in Eu/Yb superlattices.

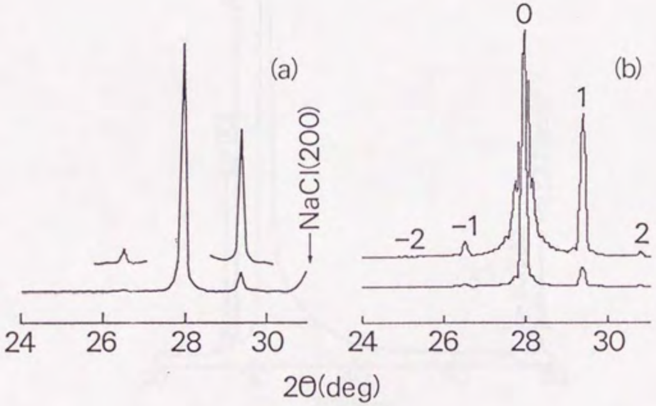

Figure 6. Measured (a) and calculated (b) middle-angle XRD patterns of a Eu (32 Å)/Yb (32 Å) superlattice.

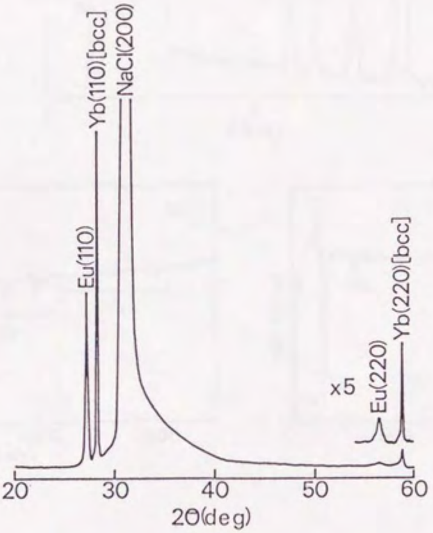

Figure 7. XRD pattern of a 1,000 Å-thick Yb film grown on an Eu buffer layer.

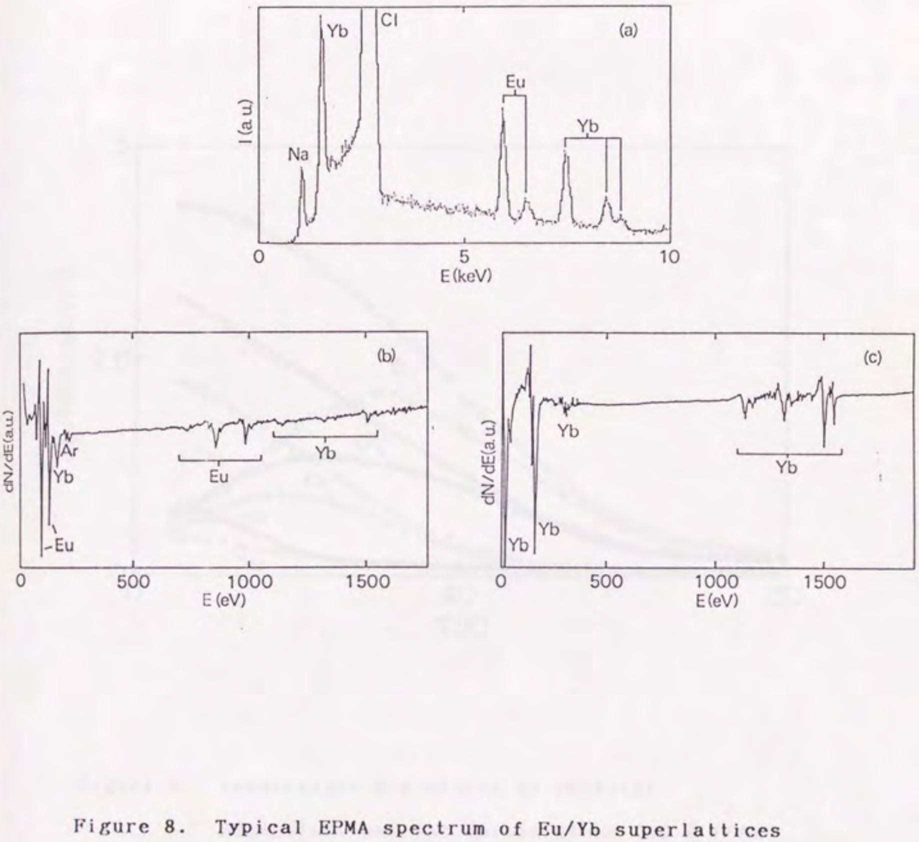

Figure 8. Typical EPMA spectrum of Eu/Yb superlattices (a), AES spectrum of Eu-rich layer (b), and AES spectrum of Yb-rich layer (c).

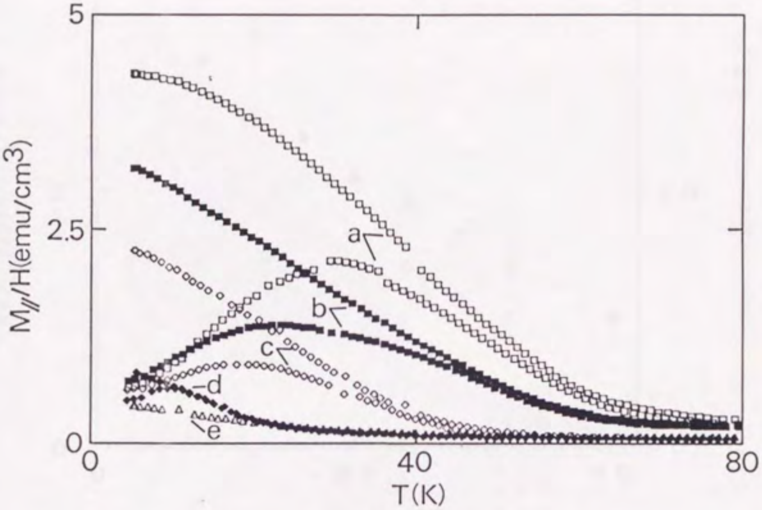

Figure 9. Temperature dependence of parallel magnetizations for epitaxial Eu (20 Å)/Yb superlattices with various Eu interlayer distances measured under 50 G for field-cooled and zero-field-cooled samples. Eu interlayer distances (Å) are 10 (a), 20 (b), 40 (c), 50 (d), and 70 (e).

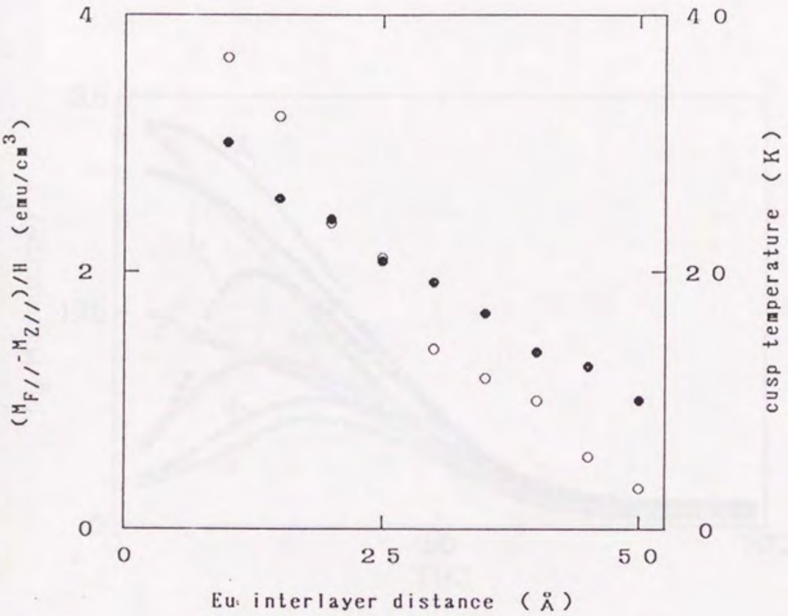

Figure 10. Thermal hysteresis (○) at 4.2 K and cusp temperature (●) versus Eu interlayer distance for epitaxial Eu (20 Å)/Yb superlattices under 50 G.

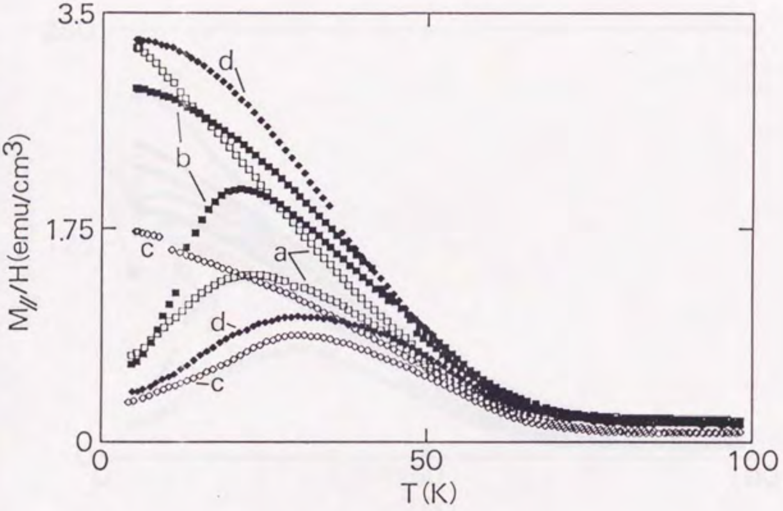

Figure 11. Temperature dependence of parallel magnetizations for epitaxial Eu/Yb (20 Å) superlattices with various Eu layer thicknesses measured under 50 G for field-cooled and zero-field-cooled samples. Eu layer thicknesses (Å) are 20 (a), 40 (b), 60 (c), and 80 (d).

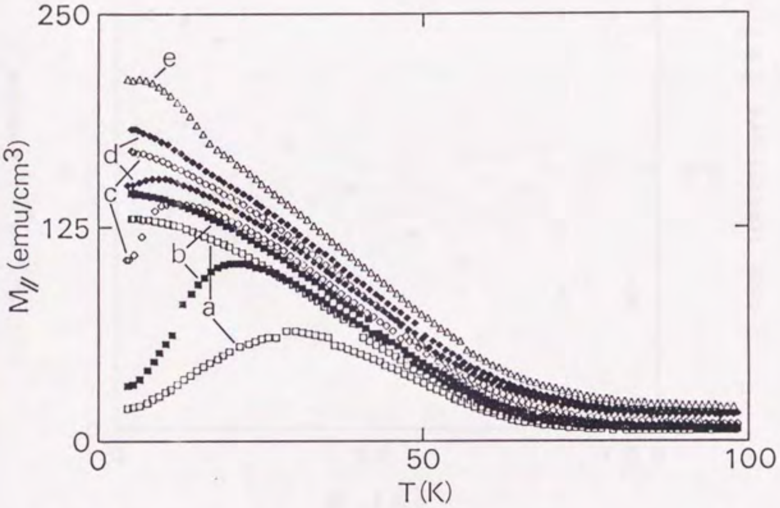

Figure 12. Temperature dependence of parallel magnetizations for epitaxial Eu (40 Å)/Yb (20 Å) superlattice measured under various magnetic-fields for field-cooled and zero-field-cooled samples. Applied magnetic-fields (G) are 30 (a), 50 (b), 100 (c), 150 (d), and 300 (e).

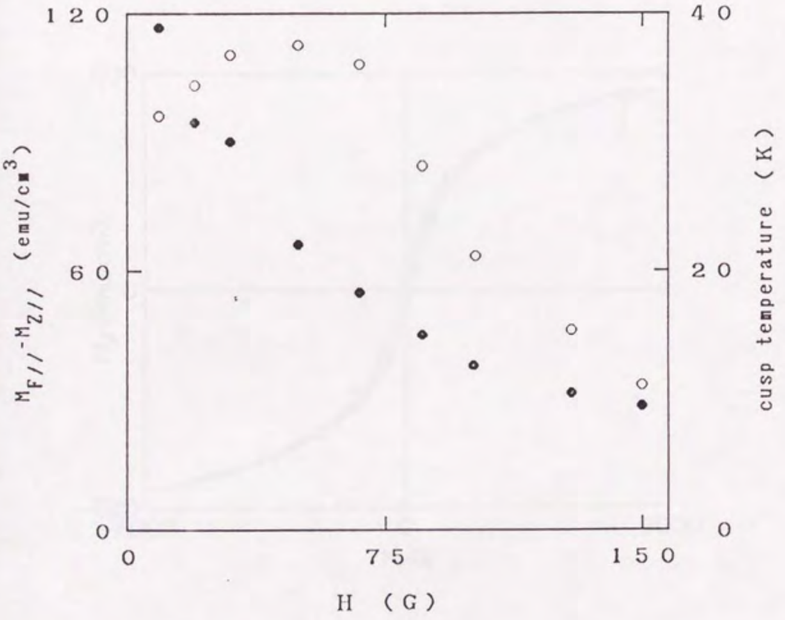

Figure 13. Thermal hysteresis (○) at 4.2 K and cusp temperature (●) versus magnetic field for epitaxial Eu (40 Å)/Yb (20 Å) superlattice.

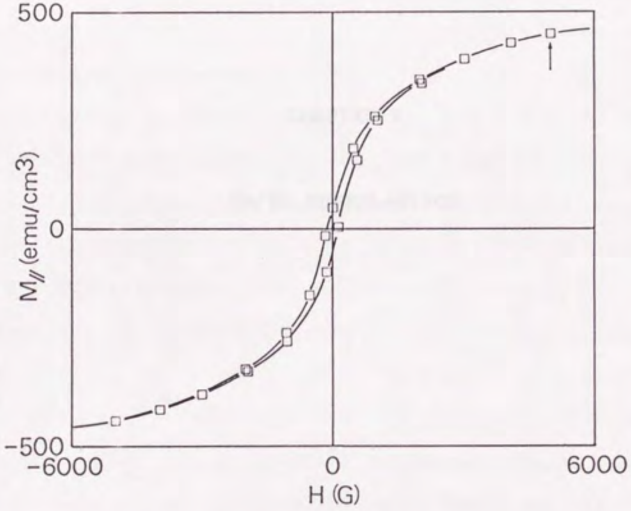

Figure 14. Parallel magnetization curve at 4.2 K for epitaxial Eu (20 Å)/Yb (40 Å) superlattice. The arrow indicates the starting point for the magnetic-field cycling on the sample which was cooled from ambient temperature to 4.2 K under 0 G.

CHAPTER V

Dy/Yb SUPERLATTICE

1. Introduction

Bulk Dy metal with hcp structure develops incommensurate helical magnetic order of the 4f spins below its Neel temperature of 178 K, and has a ferromagnetic transition at 85 K.[1] In the helical state, the wavelength increases smoothly from about 25 Å at the Neel temperature to about 40 Å just above the first-order collapse to the ferromagnetic state. Correspondingly, the turn angle per layer is 43.2 degrees at T_N and decreases to 26.5 degrees at 90 K. In the ferromagnetic phase, the easy axis is $[11\bar{2}0]$, the a-axis. It is well known that the RKKY interaction between the 4f spins, which is mediated indirectly through the polarization wave in the conduction bands, contributes significantly to this complex magnetic structure of the Dy metal. In contrast, the fcc-Yb metal which has the $4f^{14}$ configuration is believed to be non-magnetic. Here the magnetic properties of bulk alloys comprising the Dy and non-magnetic rare-earths has been studied for the Dy-Y and Dy-La systems by neutron diffraction techniques. Some interesting magnetic behavior have been observed in these alloys. For example, it has reported that $Dy_{0.95}Y_{0.05}$ alloy is effectively ferromagnetic in presence of an applied magnetic-field but that it has the helical structure in the absence of a magnetic-field.[2] The T_C of Dy-La alloy was also found to increase with increasing non-magnetic La concentration.[3] In contrast, the Dy-Yb alloy has not yet been prepared. This is because hcp-Dy metal does not give continuous solid solutions with fcc-Yb metal. Therefore, the fabrication of Dy/Yb superlattice and its structural and magnetic characteristics are very interesting targets for research. In addition, the superlattice materials comprising both metals would seem to be promising systems for investigating the modulation effects derived from a long-range interlayer exchange coupling. Because the modulation effects can be readily explored by simply varying the intervening non-magnetic Yb layer thickness while maintaining a constant magnetic Dy layer thickness. Furthermore, the superlattices, in which the Yb layer is thick enough that the interaction between Dy layers is negligible, can be considered as a pseudo two-dimensional magnetic systems.

In the present work, superlattices composed of layers of Dy and Yb metals were fabricated by means of the MBE technique. Reported here are the results from analysis of the structures and magnetic properties of the prepared Dy/Yb superlattices by RHEED, XRD, and SQUID.

2. Experimental

An NaCl single crystal, typical size 30x15x3 mm^3, was used as the substrate. The NaCl crystals were introduced to the preparation chamber as soon as their (100) planes were cleaved under ambient atmosphere. Dy (99.99 %) and Yb (99.99 %) metals were used as the source materials. Both metals were deposited at a rate of 0.2 Å/sec under ultra-high vacuum at 6×10^{-10} Torr using two Knudsen cells in an MBE apparatus. The growth temperature was kept at 290 K in order to suppress interlayer diffusion. As the first step, a 200 Å-thick Yb buffer layer was grown on a NaCl substrate having a cleaved (100) surface. Following this, the alternately deposition of the Dy and Yb metals was repeated 25 times for each sample. A 300 Å-thick Au layer was deposited on the surface of all finished samples to protect them from oxidation.

The total weight of Dy metal in the samples was determined by emission spectrochemical analysis (Nippon Jarrell-Ash ICAP-575). A solution of purified HNO_3 and HCl (1:1 volume basis) was used to dissolve the samples. Dy_2O_3 (99.99 %) was used as a reference sample for calibration.

3. Structural Characteristics

The streak patterns in the top pair of photos in Figure 1 indicate that a clean (100) surface was formed by cleavage of the NaCl single crystal. It has been found that an fcc-Yb single crystal layer can be epitaxially grown on the clean NaCl single crystal surface (see Chapter VI), as shown by the middle pair of photos in Figure 1. Prior to formation of the Dy/Yb superlattice, such an fcc-Yb buffer layer was deposited on the NaCl single crystal. An epitaxial relationship in which the Yb (100) [100] is oriented parallel to the NaCl (100) [100] is obtained because of the small lattice mismatch (2.61 %) between the fcc-Yb and NaCl crystals. The RHEED patterns of the Dy layer grown on this Yb layer were extremely complex, as shown in the bottom row of photos in Figure 1. This implies the presence of different orientations in the crystalline Dy layer. The RHEED patterns in the second Yb layer deposited on the Dy layer were the same as those shown in the second pair of photos in Figure 1. Therefore, some epitaxial relationship exists between the Yb and Dy layers. Figure 2 shows the middle-angle XRD pattern obtained for the Dy/Yb superlattice in which each layer of Dy and Yb is 40 Å-thick. Though the structure of the Dy layer could not be assigned based on the RHEED patterns, the XRD pattern reveals that the Dy metal grown on the Yb layer possessed an hcp structure with [102] and/or [110] orientation. In addition, very sharp and intense diffraction peaks could be seen in the small-angle XRD region for all of the superlattice samples. This suggests that the superlattice has grown with smooth and clear interfaces. No impurities, which can give rise to magnetism, were detected by either EPMA or AES analyses, as shown in Figures 3 (a) and (b).

4. Magnetic Characteristics

4.1 Thermal hysteresis phenomena

Thermal hystereses resulting from different cooling conditions were observed in the temperature dependence of magnetization for the Dy/Yb superlattices as shown in Figure 4. The magnetic data were obtained under 50 G for field-cooled and zero-field-cooled samples. The magnetic-frozen states, characterized by the cusp in the temperature dependent magnetization curve, were observed for zero-field-cooled superlattices. The magnetization of field-cooled superlattices ferromagnetically increased with decreasing temperature. Such thermal hystereses have been not observed in the Dy alloys containing non-magnetic rare-earth metals. It is worth noting that this unique magnetic behavior systematically changed with increasing thickness of the non-magnetic Yb layers, as shown in Figure 5. Here the thickness of the magnetic Dy layer, 40 Å, is the same in these superlattices. The thermal hysteresis, which is estimated by the difference between the magnetizations of field-cooled ($M_{F//}$) and zero-field-cooled ($M_{Z//}$) samples at 4.2 K, decreased exponentially as the Dy interlayer distance increased. In addition, the frozen temperature, as defined by the cusp position, monotonically decreased with increasing Dy interlayer distance. As a result, the thermal hysteresis and cusp were not clearly detected in Dy/Yb superlattices with Dy interlayer distances (Yb layer thicknesses) greater than 200 Å. This implies that the individual magnetic Dy layers in these superlattices are magnetically coupled to each other. Furthermore, the thermal hysteresis phenomena, including the magnetic-frozen states, are associated with the Dy interlayer interaction. Here such a long-range interaction must be a RKKY-type interaction which is mediated through the polarization wave in the conduction bands. Because the direct interaction between 4f spins which are localized in the inner core is negligibly small and is only effective over a short-range. It has been shown that the sign of the RKKY interaction alternates with the change in the distance between the magnetic spins.[4]

In superlattices, the RKKY-type interaction is modulated by the superperiodicity. Therefore, the magnetic-frozen states are likely to be produced by a combination of ferromagnetic and antiferromagnetic interlayer interactions.

Figures 6 (A) and (B) show the magnetic-field dependence of the thermal hysteresis for a Dy (40 Å)/Yb (40 Å) superlattice. With increasing magnetic-field, the $M_{F//}-M_{Z//}$ value was gradually saturated as shown in Figure 7. In addition, the frozen temperature exponentially fell with increasing magnetic-field. This shift of frozen temperature is very large and has not been observed before for spin-glass materials. In spin-glass materials, the magnetic-field dependence has been evident as a broadening of the cusp,[5] where the frozen temperature changes little during measurement under static magnetic fields.[6] Therefore it appears that the Dy/Yb superlattices are not spin-glass materials. This idea is supported by the lack of time dependent change of the magnetic states (see section 4.2) which is a characteristic normally found for spin-glass materials.[7]

The magnetic-field dependence of magnetization obtained at 4.2 K for a Dy (40 Å)/Yb (40 Å) superlattice is shown in Figure 8. The arrows indicate the starting points for the magnetic-field cycling on the samples which were cooled from ambient temperature to 4.2 K under the indicated fields. The superlattices which were cooled under magnetic-fields possessed strong magnetic anisotropy. Namely, the initial orientation of the magnetization was maintained in these samples, even though strong fields were applied in the opposite direction. This is due to the magnetocrystalline anisotropy associated with the interaction between the orbital angular momentum of 4f electron and the crystalline field of the lattice, as known in the bulk Dy metal.[8]

4.2 Spin-reorientation phenomena

When the Dy/Yb superlattices in the magnetic-frozen state indicated by "A" in Figures 9 (a), (b), and (c) were heated to a set temperature (80 (a), 100 (b), and 125 K (c)) under 50 G, the frozen states gradually melted, as shown by arrow 1 in these figures. Samples which were cooled back to 4.2 K exhibited non-reversible temperature dependence of the magnetization and formed the "B, C, and D" states (arrow 2). Here it is worth noting that the "B, C, and D" states were maintained as shown in Figure 10, even if the applied magnetic-field became zero. This indicates that spin-reorientation from the magnetic-frozen state to the ferromagnetic state occurred in the Dy/Yb superlattices. In addition, the lack of time dependent change of the magnetic states implies that the Dy/Yb superlattices are not spin-glass materials, as discussed above. When these samples, in their ferromagnetic states, were heated to set temperatures higher than the initial heating temperatures (80, 100, and 125 K) under zero-field, their magnetizations reached the frozen level at 80, 100, and 125 K, respectively, as shown by arrow 3 in Figures 9 (a), (b) and (c). Finally, the superlattices which were cooled back to 4.2 K returned to the initial magnetic-frozen state "A". The spin-reorientation behavior of Dy/Yb superlattice observed here is close to the magnetic behavior of Dy-Y alloy with high Dy concentration. Because the neutron diffraction measurements indicated that the $Dy_{0.95}Y_{0.05}$ alloy is effectively ferromagnetic in presence of an applied magnetic-field but that it has the antiferromagnetic helical structure without magnetic-field.[2]

References

[1] M. K. Wilkinson, W. C. Koehler, E. O. Wollan and J. W. Cable, J. Appl. Phys., 32, 48S (1961).

[2] H. R. Child, W. C. Koehler, E. O. Wollan and J. W. Cable, Phys. Rev., 138, A1655 (1965).

[3] W. C. Koehler, J. W. Cable, H. R. Child, R. M. Moon and E. O. Wollan, Proc. of Int. Conf. on Magnetism, Nottingham, 1964, p.271.

[4] M. Ruderman and C. Kittel, Phys. Rev., 96, 99 (1954); T. Kasuya, Prog. Theor. Phys., 16, 45 (1956); K. Yosida, Phys. Rev., 106, 893 (1957).

[5] V. Cannella and J. A. Mydosh, Phys. Rev. B 6, 4220 (1972).

[6] B. Barbara, A. P. Malozemoff and Y. Imry, Physica B 108, 1289 (1981).

[7] C. N. Guy, J. Phys. F 8, 1309 (1978).

[8] S. Chikazumi, S. Tanuma, I. Oguru, F. Ono and K. Tajima, IEEE Trans. Magn. MAG-5, 265 (1969).

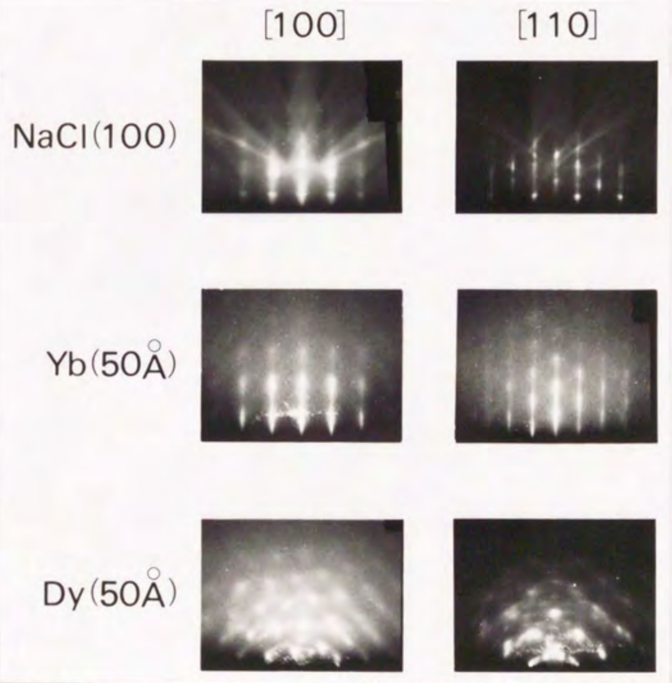

Figure 1. RHEED patterns of cleaved NaCl (100) surface, Yb buffer layer grown on NaCl substrate, and Dy layer grown on a Yb buffer layer.

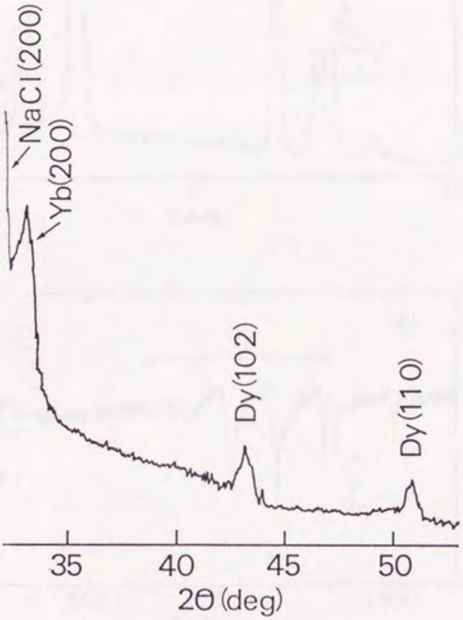

Figure 2. Middle-angle XRD pattern of a Dy (40 Å)/Yb (40 Å) superlattice.

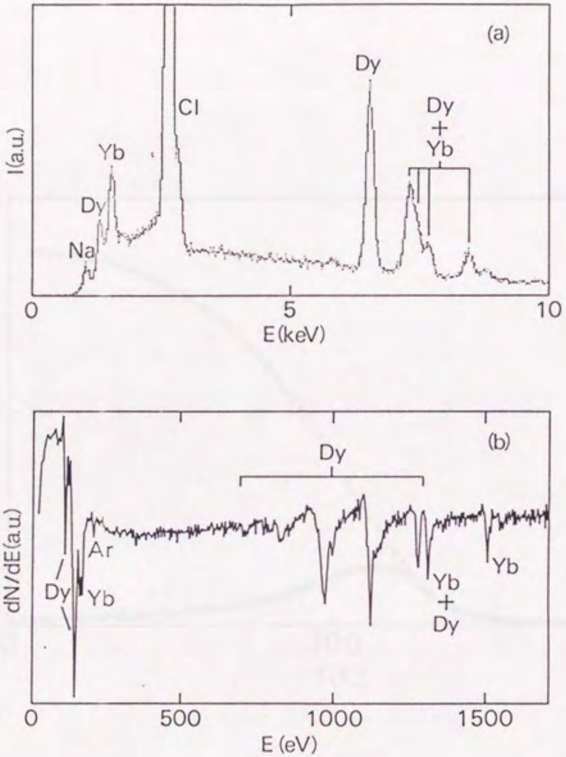

Figure 3. Typical EPMA (a) and AES (b) spectra of Dy/Yb superlattices.

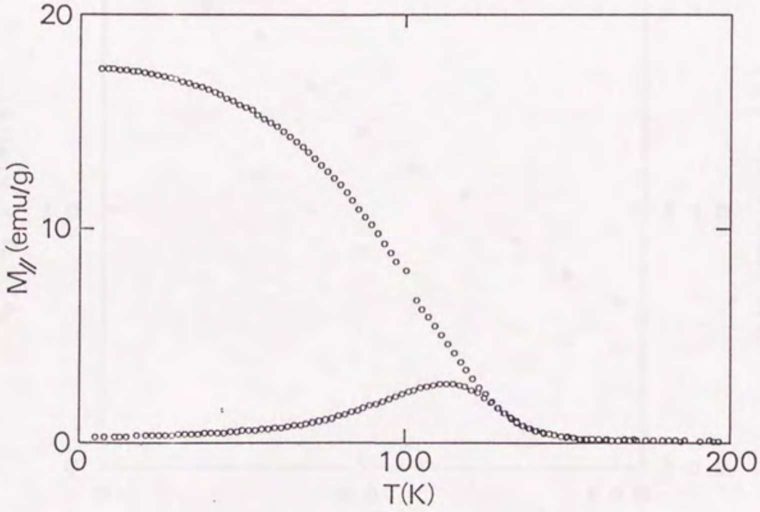

Figure 4. Temperature dependence of parallel magnetizations for Dy (40 Å)/Yb (40 Å) superlattice measured under 50 G for field-cooled and zero-field-cooled samples.

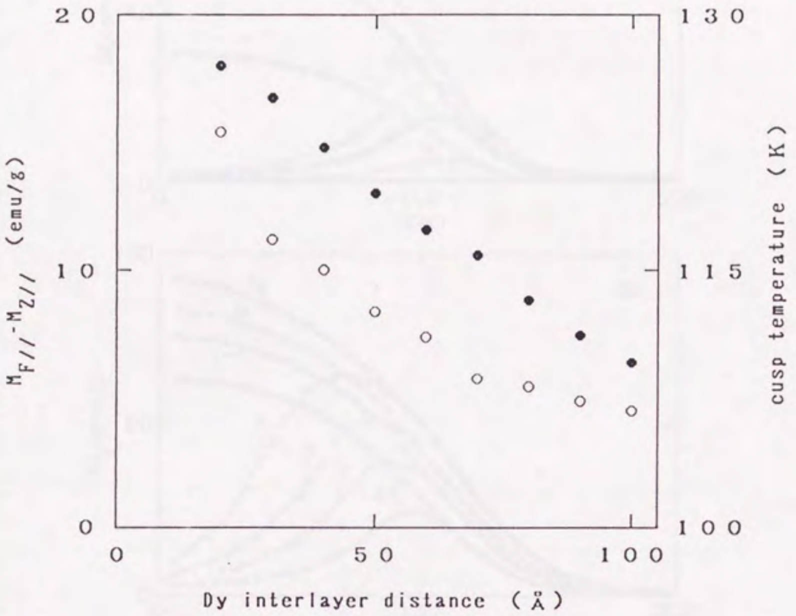

Figure 5. Thermal hysteresis (○) at 4.2 K and cusp temperature (●) versus Dy interlayer distance for Dy (40 Å)/Yb superlattices under 50 G.

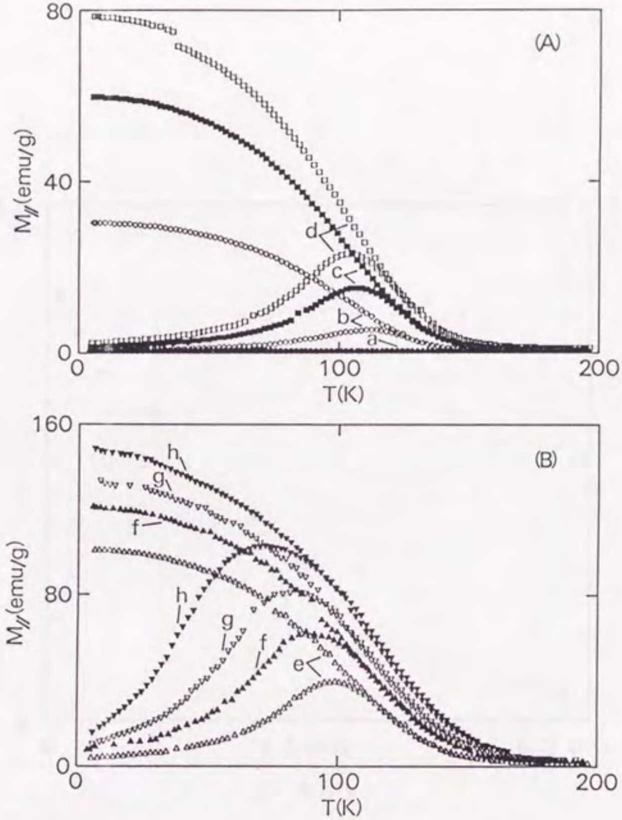

Figure 6. Temperature dependence of parallel magnetizations for Dy (40 Å)/Yb (40 Å) superlattice measured under various magnetic-fields for field-cooled and zero-field-cooled samples. Applied magnetic-fields (G) are a: 0, b: 100, c: 300, d: 500 in figure (A) and e: 1,000, f: 2,000, g: 3,000, h: 5,000 in figure (B).

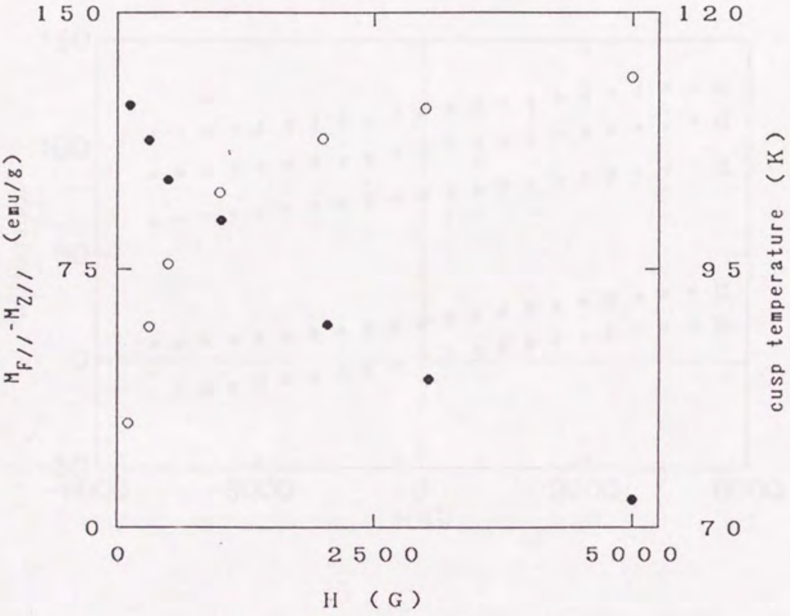

Figure 7. Thermal hysteresis (○) at 4.2 K and cusp temperature (●) versus magnetic field for Dy (40 Å)/Yb (40 Å) superlattice.

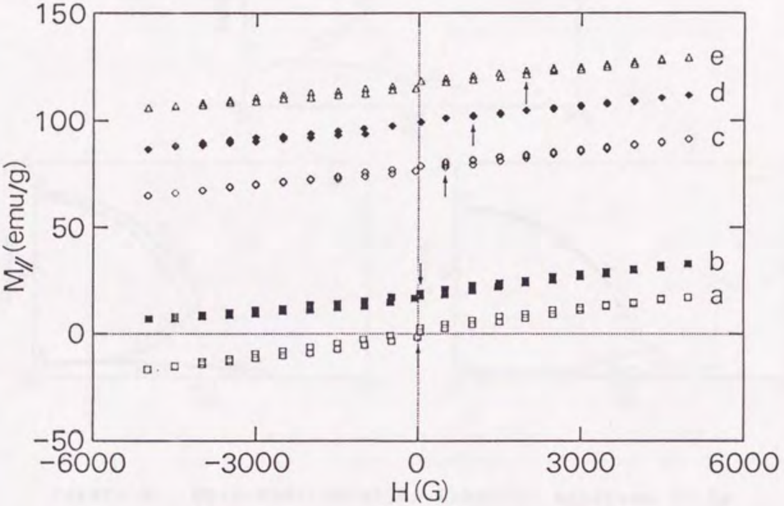

Figure 8. Dependence of Dy (40 Å)/Yb (40 Å) superlattice magnetizations at 4.2 K on magnetic-field cycling. The arrows indicate the starting points for the magnetic-field cycling on the samples which were cooled from ambient temperature to 4.2 K under various magnetic-fields (a: 0, b: 50, c: 500, d: 1,000, and e: 2,000 G).

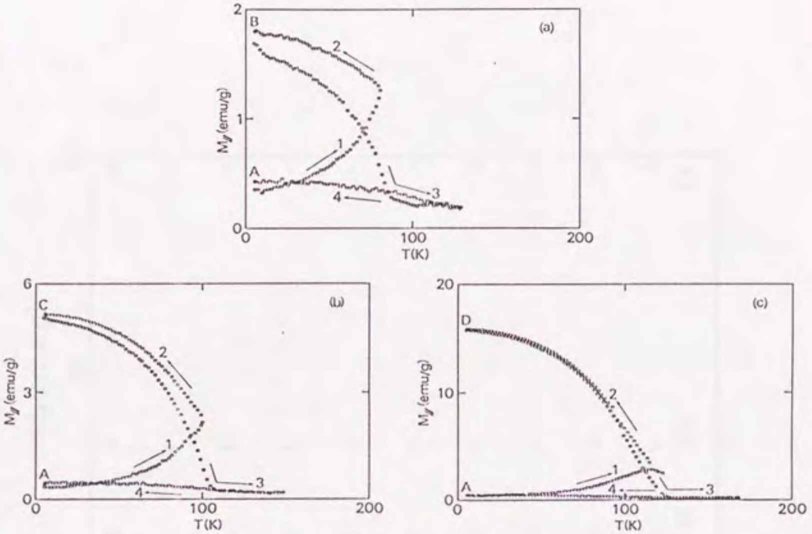

Figure 9. Spin-reorientation behavior observed in Dy (40 Å)/Yb (40 Å) superlattice. Samples in the "A" state were initially heated to set temperatures, 80 (a), 100 (b), and 125 K (c), under 50 G as shown by arrow 1. These were cooled back to 4.2 K to form the "B, C, and D" states (arrow 2). Next the samples were heated to temperatures higher than 80 (a), 100 (b), and 125 K (c), under zero-field as shown by arrow 3 and finally cooled back to 4.2 K (arrow 4).

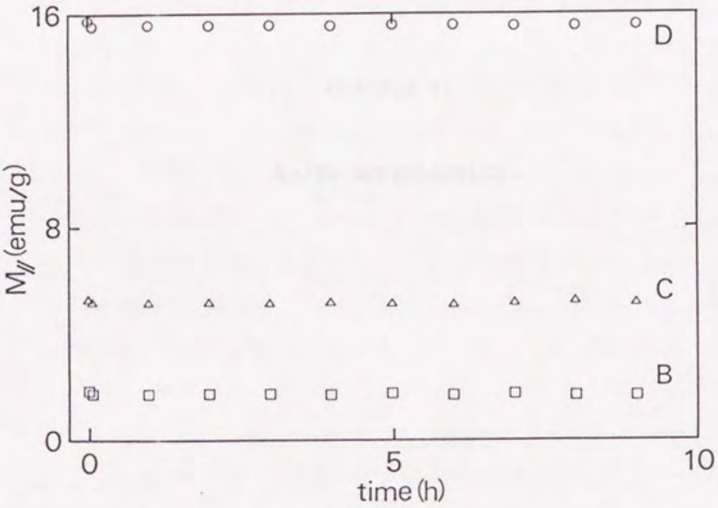

Figure 10. Time dependence of magnetized state stability under zero-field in Dy (40 Å)/Yb (40 Å) superlattices with "B, C, and D" states.

CHAPTER VI

Sm/Yb SUPERLATTICE

1. Introduction

The rhombohedral crystal structure of Sm is quite complicated, and consists of a nine-layer stacking sequence ABABCBCAC... of hexagonal close-packed layers (with domains of the inverse sequence ACACBCBAB... coexisting in the structure), as shown in Figure 1.[1] The B and C sites have hexagonal near neighbor environments, while A sites have cubic environments. On the other hand, Yb metal possesses the fcc structure (a_{Yb}=5.481 Å) under ambient temperature and pressure.[1] Assuming that the structure of Sm transforms from the rhombohedral phase to the fcc phase, in which the most densely close-packed state of the Sm atoms does not change, the cubic constant, a_{Sm}, of the fcc-Sm can be estimated from the relation $a_{Sm}=\sqrt{2} \times a_{hcp}$ using the lattice constant, a_{hcp}, of the rhombohedral Sm phase (see Figure 1). The lattice constant thus calculated for fcc-Sm metal, a_{Sm}=5.132 Å, is close to that of the fcc-Yb phase. Therefore, it appeared promising to obtain the fcc-Sm phase by epitaxially growing a thin Sm layer on a fcc-Yb metal layer. It also appeared possible to prepare a superlattice system consisting of fcc-Sm and fcc-Yb layers. A Sm-Yb alloy has never yet prepared because Sm metal does not give continuous solid solutions with Yb metal. Thus, the fabrication of Sm/Yb superlattices and analysis of their structural characteristics appeared to be very interesting targets for this research.

From this point of view, Sm/Yb superlattices with various periods were investigated. Reported here are the formation of Sm/Yb superlattices prepared using the MBE method and their structure as elucidated by RHEED, TED, and XRD.

2. Experimental

An NaCl single crystal, typical size 30x15x3 mm^3, was used as the substrate. The NaCl crystals were introduced to the preparation chamber as soon as their (100) planes were cleaved under ambient atmosphere. Sm (99.99 %) and Yb (99.99 %) metals were used as the source materials. Both metals were deposited at a rate of 0.15 Å/sec under ultra-high vacuum at 9x10^{-10} Torr using two Knudsen cells in an MBE apparatus. The growth temperature was kept at 290 K in order to suppress interlayer diffusion. As the first step, a 200 Å-thick Yb buffer layer was grown on a NaCl substrate having a cleaved (100) surface. Following this, the Sm and Yb metals were alternately deposited. The period of the superlattice was repeated 25 times for each sample. A 300 Å-thick Au layer was deposited on the surface of all finished samples in order to protect them from oxidation.

3. Structural Characteristics

3.1 RHEED and TED analyses

Typical RHEED patterns of a cleaved NaCl (100) surface in two incident azimuths are shown in the top pair of photos in Figure 2. The streak patterns indicate that a clean (100) surface was formed by the cleavage. Yb was first deposited onto this NaCl (100) surface to form a buffer layer for the preparation of the Sm/Yb superlattice. The RHEED patterns of a 200 Å-thick Yb layer, observed for the same azimuthal angles as those of NaCl, are shown in the second pair of photos from the top. The left and right patterns can be attributed to fcc-Yb (100) [100] and [110], respectively. This experimental result indicates that the Yb layer was epitaxially grown as a single crystal on the NaCl substrate. Here the existence of an epitaxial relationship between the Yb (100) [100] and NaCl (100) [100] is due to the small lattice mismatch, 2.61 %, between the fcc-Yb and NaCl crystals. The RHEED patterns from a 50 Å-thick Sm layer grown on the Yb buffer layer are seen to have the same symmetry as fcc-Yb and similar spacing in two of the principal crystallographic directions on the (100) face. The fact that spots and not streaks were produced in the RHEED patterns indicates that the crystal growth of Sm metal is dominated by three-dimensional nucleation which is atomically rough, but nevertheless forms a single crystal. This observation, however, does not prove that the stacking sequence of Sm is fcc. Therefore, TED analysis was carried out on this system. Figure 3 shows the TED patterns observed for a 200 Å-thick Sm layer grown on a Yb buffer layer. Pattern (a) was taken with the incident beam perpendicular to the substrate. On the other hand, pattern (b) was observed when the sample was slanted. From the symmetry and the ratio of distances between diffraction spots, the (a) and (b) patterns can be assigned as the [100] and [310] azimuth, respectively, of the fcc crystal. Since there are no other phases present except for the fcc phase, the Sm metal grown on the Yb buffer layer is concluded to possess an fcc structure.

3.2 XRD analysis

All of the superlattice samples showed very sharp and intense diffraction peaks in their small-angle XRD patterns, as shown in Figure 4. These corresponded to their superlattice periodicities. Moreover, the designed superlattice periodicity (D/N) and the superlattice spacing (Λ) determined from XRD were in good agreement as shown in Figure 5, where D is the total thickness of the prepared superlattice and N the total number of the Sm (or Yb) layers. This indicates that the epitaxial Sm/Yb superlattices, in which interdiffusion was probably insignificant, were successfully grown on the Yb buffer layer formed on NaCl (100). Figure 6 (a) shows the middle-angle XRD pattern obtained for the Sm/Yb superlattice in which each layer of Sm and Yb is 53 Å-thick. Here the x-ray diffraction simulation using a "statistical model (see Section 2.2 of Chapter II)" was carried out to obtain information on the structural parameters, such as interface diffusion and coherence length, of the superlattices. The values of the parameters in which the calculated spectrum was in agreement with the experimental spectrum, as shown in Figure 6 (b), suggested that the thickness of the inter-diffused layer and the structural coherence length were 5 atomic-layers and 7 "unit cells", respectively. The "unit cell" means one period of the superlattice. In Figure 6, very sharp peaks observed at 2θ =32.9 and 34.7 degrees (indicated by 0' and 0) should correspond to the average (100) spacings of fcc-Yb and fcc-Sm layers in the superlattice. Other peaks are satellites in relation to the superperiodicity. These results imply that the fcc structure of the Sm layer, confirmed by the RHEED and TED observation, was formed and stabilized because of the epitaxial relationship with the fcc-Yb layer. To date, the rhombohedral structure (see Figure 1) has been observed as the ambient temperature and pressure phase of Sm metal. The bcc and hcp phases have been formed under high temperature and/or pressure.[1] Therefore, the fcc structure of Sm metal observed here can be concluded to be a new metastable phase. The EPMA and AES measurements indicated that this unique structure was not due to impurities, as shown in Figures 7 (a) and (b).

In order to examine the critical thickness of the epitaxial growth of the fcc-Sm layer, that is, the thickness above which the structure of the deposited Sm changes to the rhombohedral ambient temperature phase, Sm layers were deposited up to thicknesses of 3,000 Å on a 500 Å-thick fcc-Yb buffer layer epitaxially grown on NaCl (100). XRD patterns of Sm films with various thicknesses grown on Yb buffer layer are shown in Figure 8. A new diffraction peak which can not be assigned in the known Sm and Yb crystals, including high temperature and pressure phases, was clearly seen at about $2\theta = 35.1$ degrees on NaCl (200) and Yb (200). Since the intensity of this new peak increases with increasing thickness of the Sm layer, this diffraction corresponds to the fcc-Sm lattice. The RHEED patterns observed for the 3,000 Å-thick Sm film also showed the same symmetry as that of the fcc-Yb buffer layer and 50 Å-thick Sm layer, as shown in the bottom step of Figure 2. Therefore, it is concluded that the Sm layer possesses the fcc structure at least up to 3,000 Å when it is epitaxially grown on an fcc-Yb layer. Note that this thickness is large enough to be considered almost the same as the bulk state. The cubic lattice constant (a_0) was determined to be 5.11± 0.01 Å using the XRD data obtained on a number of different Sm films with 3,000 Å thickness. This lattice constant is close to the value of 5.132 Å estimated from the relation $a_{Sm}=\sqrt{2}\times a_{hcp}$ using the lattice constant of the rhombohedral Sm. This means that the most densely close-packed state of the Sm atoms changes little when the structure transforms from the rhombohedral phase to the fcc phase.

It is generally considered to be impossible to fabricate a thick film composed of a non-thermodynamic metal phase by utilizing the epitaxial relationship. This is because the stabilization effect by the epitaxial relationship decreases on increasing the distance from the interface. In fact, bcc-Zr,[2] fcc-Fe,[3] fcc-Mn,[4] fcc-Co,[5] and hcp-Fe[6] high temperature and/or high pressure phases were reported to be stable only up to a few tens of Å, above which the structures of these metals changed to the phase which is stable at room temperature. In this respect, the Sm-Yb system seems to be rather exceptional. Seemingly, there exists, by some reason, an especially strong epitaxial relationship between fcc-Sm and fcc-Yb layers. The fact that all samples prepared in the present study exhibited an extremely high crystallinity in the fcc-Sm layer, although the growth temperature was as low as 290 K, might also be related to the strong epitaxial interaction between Sm and Yb layers.

References

[1] B. J. Beaudry and K. A. Gschneidner, Jr., in Handbook of the Physics and Chemistry of the Rare Earths, edited by K. A. Gschneidner, Jr. and L. Eyring (North-Holland, Amsterdam, 1978), Vol. 1, p. 173-232.

[2] W. P. Lowe and T. H. Geballe, Phys. Rev. B 29, 4961 (1984).

[3] D. A. Steigerwald and W. F. Egelhoff, Jr., Sur. Sci., 192, L887 (1987).

[4] Y. Nishihata, M. Nakayama, N. Sano and H. Terauchi, J. Appl. Phys., 63, 319 (1987).

[5] F. J. Lamelas, C. H. Lee, H. He, W. Vavra and R. Clarke, Phys. Rev. B 40, 5837 (1989).

[6] M. Maurer, J. C. Ousset, M. F. Ravet and M. Piecuch, Europhys. Lett., 9, 803 (1989).

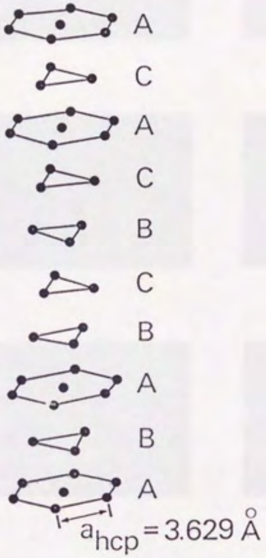

Figure 1. Structure of the ambient temperature Sm phase.

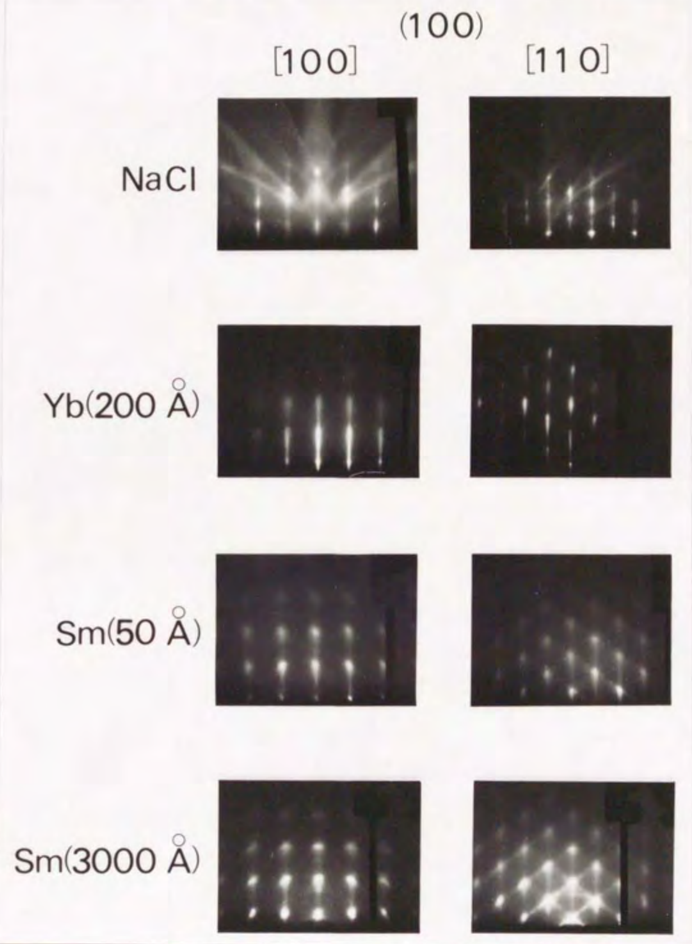

Figure 2. RHEED patterns of cleaved NaCl (100) surface, Yb buffer layer grown on NaCl substrate, and 50 Å and 3,000 Å-thick Sm layers grown on a Yb buffer layer.

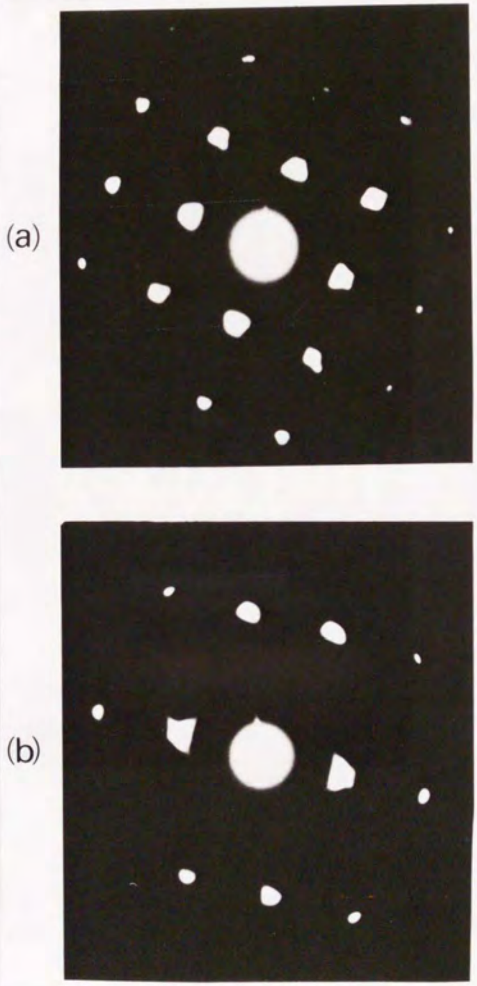

Figure 3. TED patterns of a 200 Å-thick Sm layer grown on a Yb buffer layer: fcc-[100] (a) and fcc-[310] (b).

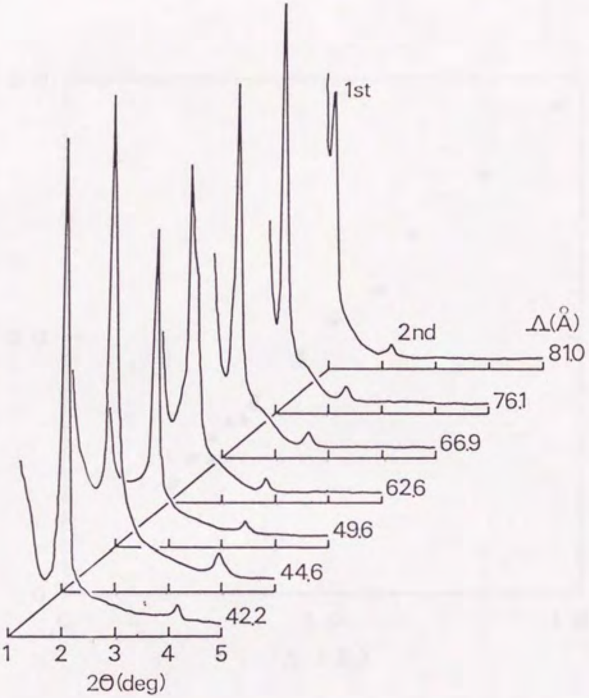

Figure 4. Small-angle XRD patterns of Sm/Yb superlattices with various superlattice periodicities (Λ).

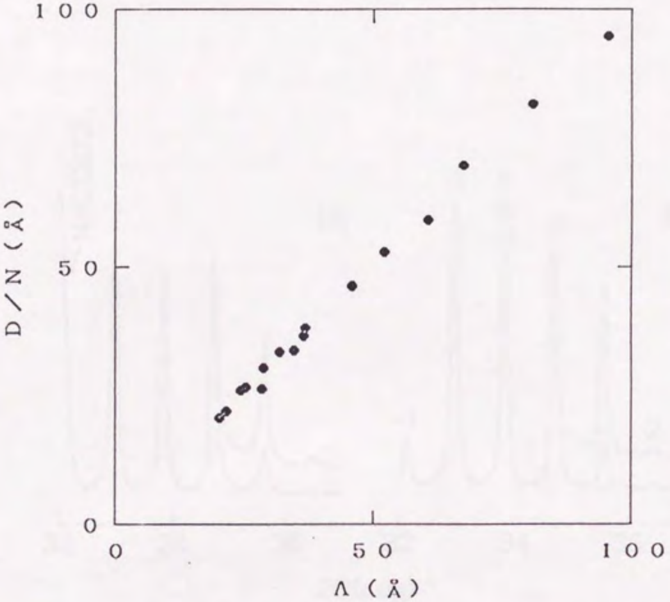

Figure 5. Comparison between the designed (D/N) and observed (Λ) modulation wavelengths in Sm/Yb superlattices.

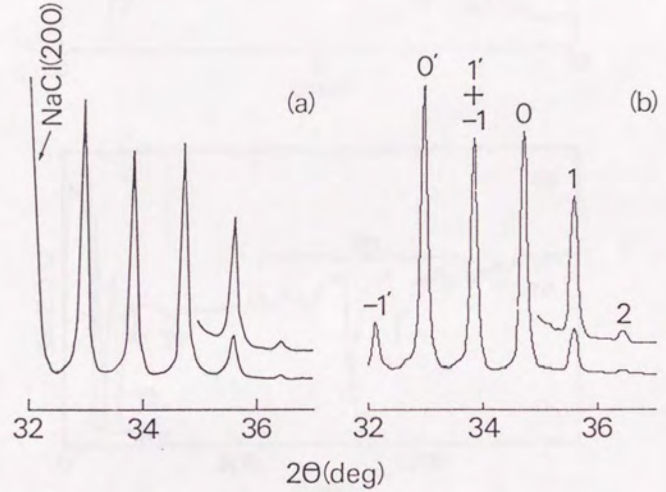

Figure 6. Measured (a) and calculated (b) middle-angle XRD patterns of a Sm (53 Å)/Yb (53 Å) superlattice.

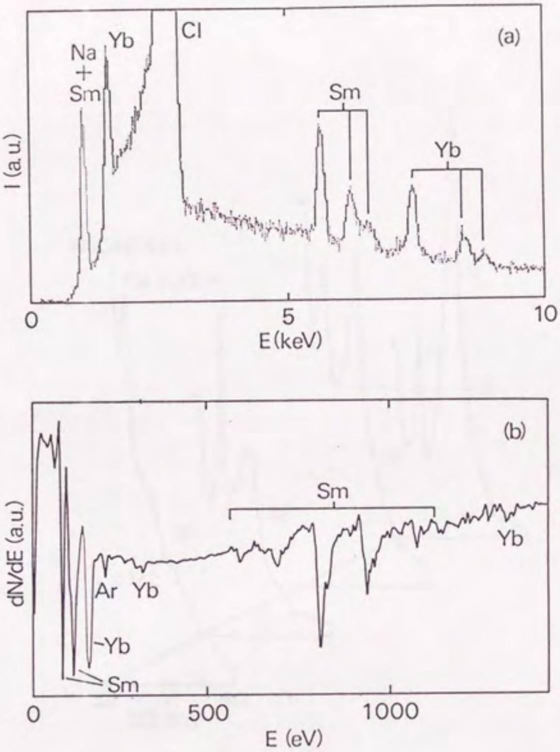

Figure 7. Typical EPMA (a) and AES (b) spectra of Sm/Yb superlattices.

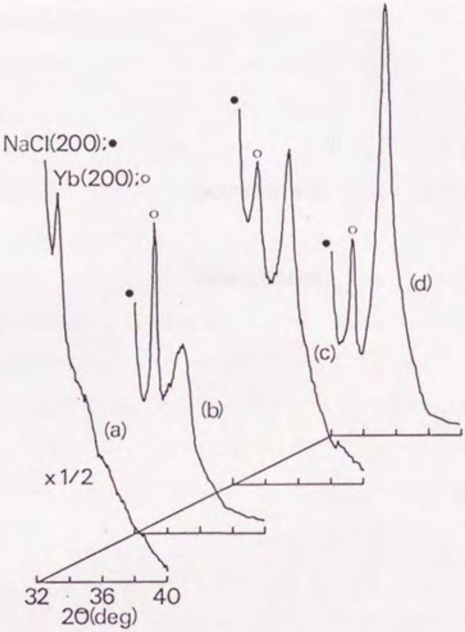

Figure 8. XRD patterns of Sm films with various thicknesses grown on a 500 Å-thick Yb layer: 200 (a), 500 (b), 1,000 (c), and 1,500 Å (d).

CHAPTER VII

CONCLUSION

In the Eu/Yb superlattices, the Yb layers were found to be in the bcc structure, high temperature phase, as described in Chapter IV. It was also shown that the bcc-Yb can be epitaxially grown on the bcc-Eu layer up to a thickness of 1,500 Å. In Chapter VI, it was shown that fcc-Sm, a new metastable phase, can be stabilized by the epitaxial relationship with fcc-Yb. In addition, it was confirmed that the Sm layer possesses the fcc structure at least up to 3,000 Å when it is epitaxially grown on an fcc-Yb layer. The non-thermodynamic structures of Yb and Sm were stable even up to thickness large enough that the material could be considered to be in a bulk state. Other non-thermodynamic metals have been reported to be stable only up to a few tens of Å. Normally, the stabilization effect by the epitaxial relationship should decrease on increasing the distance from the interface. Therefore, the Eu-Yb and Sm-Yb systems are the first two examples that show the possibility of fabricating by the MBE technique a thick metal layer having a non-thermodynamic structure. Here the question remains as to why the non-thermodynamic bcc-Yb and fcc-Sm crystals were the only materials to be stabilized in their bulk states. Bulk crystals of Yb and Ce metals are known to possess unique structural characteristics. In the case of Yb metal, the hcp structure formed by cooling to 4.2

K is maintained even if it is heated back to ambient temperature.[1] In addition, Ce can exist at atmospheric temperature and pressure in the fcc (γ) form and undergoes an isostructural transition near 100 K to another fcc form referred to as α -Ce, accompanied by about a 17 % volume decrease. Here it is worth noting that this $\gamma - \alpha$ transition does not reoccur at the same temperature.[2] The valence of Yb and Ce fluctuate between 2 and 3, and 3 and 4 in their metal states. It has been reported that the unique structural aspects of Yb and Ce metals are likely to be associated with the valence fluctuation of each metal.[3,4] Here it is found that the valence of Sm metal fluctuates between 2 and 3. Therefore, the epitaxial growth of the thick non-thermodynamic bcc-Yb or fcc-Sm metal film observed is also likely to be associated with the valence fluctuation characteristics of both metals. This idea is supported by the experimental result that no epitaxial growth of the non-thermodynamic phase was observed for the Dy metal whose valence is stable at 3.

Thermal hysteresis resulting from different cooling conditions was observed in the magnetic properties of the Eu/Mn, Eu/Yb, and Dy/Yb superlattices with short periodicity, as described in Chapters III, IV, and V. Namely, the zero-field-cooled samples were in a magnetic-frozen state, characterized by the clear cusp in the temperature dependent magnetization curve, at low temperature. The magnetization of the field-cooled samples increased as the temperature decreased. Such thermal hystereses became more distinct with decreasing distance between the magnetic rare-earth layers in the superlattices containing non-magnetic Yb metal. This result indicates that the individual magnetic rare-earth metal layers in these superlattices can be magnetically coupled to each other and the thermal hysteresis phenomena including the magnetic-frozen states observed are associated with the rare-earth interlayer interaction, such as Eu-Eu or Dy-Dy. Here the long-range interaction must be a RKKY-type interaction which is mediated by the 5d and/or 6s conduction electrons of the rare-earth metals because the direct interaction between 4f spins which are localized in the inner core is negligibly small and is only effective over a short-range. It has been shown that the sign of the RKKY-type interaction alternates with the change in the distance between the magnetic spins. In the superlattices described here, the RKKY-type interaction is modulated by the superperiodicity. Therefore, the magnetic-frozen states are likely to be produced by a combination of ferromagnetic and antiferromagnetic interlayer interactions. In addition, since there was no time dependence observed for the magnetic states of any of the superlattices, the observed magnetism is associated with the inherent nature of rare-earth superlattices and not a spin-glass characteristic.

Though the Eu/Yb and Dy/Yb superlattices possessed thermal hystereses in their magnetic properties similar to that observed for the Eu/Mn superlattice as described above, only one cusp was present in the temperature dependent magnetization curves of the Yb containing superlattices. In contrast, the three cusps were observed for the Eu/Mn superlattices under low field. The difference in magnetic properties between Eu/Mn and the other superlattices is likely to occur because Mn is magnetic and Yb is non-magnetic. It was concluded that the long-range interlayer interaction between magnetic rare-earth layers such as Eu or Dy contributed to the thermal hysteresis phenomena. This is the same, however, for all three superlattices (Eu/Mn, Eu/Yb, and Dy/Yb) and cannot account for the appearance of multiple cusps in Eu/Mn superlattices. In addition, the amorphous structure of Eu/Mn superlattices is not related to the difference in magnetic properties between Eu/Mn and other superlattices because the amorphous Eu/Yb superlattices which were prepared at a growth temperature of 90 K possessed only one cusp in the temperature dependent magnetization curve. Sharp reflections up to 5th-order corresponding to the superperiodicity were seen in the small-angle XRD patterns of Eu/Mn superlattices, whereas reflections up to only second-order were identified for the Eu/Yb superlattices. This implies that the interfaces of Eu/Mn superlattices are smoother than those of Eu/Yb superlattices. Therefore, the interlayer diffusion in the superlattice structures also cannot account for the appearance of multiple cusps. Thus, the presence of the magnetic Mn layer which produces an interfacial interaction between the Mn and Eu layers is likely to be the source of the multiple cusps observed for the Eu/Mn superlattices. Such an interfacial interaction is not observed in the superlattices containing non-magnetic Yb metal.

In the Eu/Yb superlattices, the $M_{F//}-M_{Z//}$ value corresponding to the magnitude of thermal hysteresis was saturated until the magnetic-field reached 50 G, above which point it exponentially decreased. As a result, the thermal hysteresis was not observed above 4.2 K under 300 G in the Eu/Yb superlattices. In contrast, such a critical field for the Dy/Yb superlattices was found to be higher than that of the Eu/Yb superlattices because the hysteresis in Dy/Yb superlattices was clearly obtained under strong magnetic-fields as high as 5,000 G. This difference in magnetic properties between Dy/Yb and Eu/Yb superlattices is likely to be due to the difference in strength of the interlayer interaction, such as Dy-Dy or Eu-Eu, which contributes to the thermal hystereses. This appears reasonable because the magnetic transition temperature of bulk Dy metal (179 K^5) is higher than that of bulk Eu metal (91 K^6).

The hysteresis loops obtained for the zero-field-cooled Eu/Mn superlattices were symmetrical. In contrast, anti-symmetrical hysteresis loops were observed for the field-cooled Eu/Mn superlattices. This indicates that unidirectional anisotropy exists in this system. On the other hand, the Eu/Yb superlattices did not possess the unidirectional anisotropy. Therefore, the unidirectional anisotropy in the Eu/Mn superlattices is expected to arise from the Eu-Mn interfacial interaction. The hysteresis loop measurement indicated that the field-cooled Dy/Yb superlattices possessed strong magneto-crystalline anisotropy. That is, the initial orientation of the magnetization was maintained in these samples, even though strong fields as high as 5,000 G were applied in the opposite direction. This is due to the interaction between the orbital angular momentum of 4f electron and the crystalline field of the lattice. This idea is supported by the experimental results that no magneto-crystalline anisotropy was observed in the superlattices containing Eu metal whose orbital angular momentum for the ground state, $^8S_{7/2}$, is zero.

In the present study, the following three points were set as research aims:

(1) Atomic-scale control of metallic superlattice structure.

(2) Confirmation of unique magnetism arising from artificial compositional modulation and reduced dimensionality.

(3) Stabilization of non-thermodynamic metal phases using the epitaxial relationship at superlattice interfaces.

The MBE method was extremely effective in meeting the first aim of allowing film growth to be controlled to the monolayer level. This was demonstrated by the epitaxial growth of the Eu/Yb and Sm/Yb superlattices. The long-range character of the magnetic interaction in the rare-earth metals allowed the second aim to be realized. Namely, the unique thermal hysteresis phenomena including magnetic-frozen states associated with the interlayer interaction between magnetic rare-earth layers were observed in the Eu/Mn, Eu/Yb, and Dy/Yb superlattices. In addition, the third aim of epitaxially growing non-thermodynamic metal phases was successfully achieved using the MBE technique to grow the Eu-Yb and Sm-Yb systems.

References

[1] S. Tanuma, W. R. Datars, H. Doi, and A. Dunsworth, Solid State Commun., 8, 1107 (1970).

[2] D. C. Koskenmaki and K. A. Gschneidner, Jr., in Handbook of the Physics and Chemistry of the Rare Earths, edited by K. A. Gschneidner, Jr. and L. Eyring (North-Holland, Amsterdam, 1978), Vol. 1, p. 337-378.

[3] G. Johansen and A. R. Mackintosh, Solid State Commun., 8, 121 (1970).

[4] R. Ramirez and L. M. Falicov, Phys. Rev. B 3, 2425 (1971).

[5] R. M. Bozorth and J. H. Van Vleck, Phys. Rev., 118, 1493 (1960).

[6] D. R. Behrendt, S. Legvold and F. H. Spedding, Phys. Rev., 109, 1544 (1958).

APPENDIX I

LIST OF PAPERS PUBLISHED IN RELATION TO THE PRESENT STUDY

[1] ·Dipole-Dipole Interaction in the Diffused Interlayer of Magnetic Superlattices
·Atsushi Maeda and Haruo Kuroda
·Thin Solid Films, 161, L83 (1988)

[2] ·Structural and Magnetic Studies of an Artificial Eu/Mn Superlattice
·Atsushi Maeda, Tohru Satake, Toshinari Fujimori, Hiroyuki Tajima, Mototada Kobayashi and Haruo Kuroda
·Journal of Applied Physics, 65, 3845 (1989)

[3] ·Magnetic-Frozen States in Eu/Mn Superlattices
·Atsushi Maeda, Tohru Satake, Toshinari Fujimori and Haruo Kuroda
·Journal of Physics, 2, 245 (1990)

[4] ·体心立方Ｅｕ／Ｙｂ超格子のエピタキシャル成長
－ Ｙｂ金属高温相の安定化 －
·前田篤志，佐竹徹，藤森俊成，黒田晴雄
·日本応用磁気学会誌，14, 359 (1990)

[5] ·Structural and Magnetic Characteristics of Eu/Mn and Eu/Yb Superlattices Prepared by the MBE Technique
·Atsushi Maeda, Tohru Satake, Toshinari Fujimori and Haruo Kuroda
·Vacuum, 41, 1251 (1990)

[6] ·Epitaxial Growth of bcc-Eu/Yb Superlattices
·Atsushi Maeda, Tohru Satake, Toshinari Fujimori and Haruo Kuroda
·Journal of Applied Physics, 68, 3246 (1990)

[7] ·In Situ Electron Beam Irradiation Induced In-Plane Orientation of Europium Thin Film Grown by the Molecular Beam Epitaxy Technique
·Atsushi Maeda, Tohru Satake, Toshinari Fujimori, Shigeru Maeda and Haruo Kuroda
·Thin Solid Films, 192, 135 (1990)

[8] ·Thermal Hysteresis Phenomena in Eu/Yb Superlattices
·Atsushi Maeda, Tohru Satake, Toshinari Fujimori and Haruo Kuroda
·Journal of Physics, 3, 1967 (1991)

[9] ·Ｄｙ／Ｙｂ人工格子の構造と磁性
·前田篤志，佐竹徹，藤森俊成，黒田晴雄
·日本応用磁気学会誌，15，441 (1991)

[10] ·Epitaxial Growth of fcc-Sm/Yb Artificial Superlattices
·Atsushi Maeda, Tohru Satake, Toshinari Fujimori and Haruo Kuroda
·Journal of Applied Physics, 69, 6417 (1991)

[11] ·Spin-Reorientation Phenomena in Dy/Yb Superlattices
·Atsushi Maeda, Tohru Satake and Haruo Kuroda
·Journal of Physics, 3, 5241 (1991)

[12] ·Magnetic-Field Dependence of Eu/Mn Superlattices
·Atsushi Maeda, Tohru Satake and Haruo Kuroda
·Physics Letters A, 157, 178 (1991)

APPENDIX II

LIST OF OTHER PAPERS PUBLISHED

[1] ·Preparation and X-Ray Crystal Structure (for Ln=Sm) of (μ-phthalocyaninato)bis[di(2,2,6,6-tetramethylheptane-3,5-dionato)$\mathrm{Ln}^{\mathrm{III}}$] (Ln=Sm, Eu, Gd, Tb, Dy, Ho, Er, Tm, Yb, and Y)
·Hiroshi Sugimoto, Teruaki Higashi, Atsushi Maeda, Masayasu Mori, Hideki Masuda and Tooru Taga
·Journal of the Chemical Society, Chemical Communications, 1234 (1983)

[2] ·Mixed-Ligand Rare Earth Complexes of Phthalocyanine and β-Diketones
·Hiroshi Sugimoto, Teruaki Higashi, Atsushi Maeda, Yasumasa Hirai, Junji Teraoka and Masayasu Mori
·Journal of the Less-Common Metals, 112, 387 (1985)

[3] ·Intramolecular Exchange Interaction between Two Rare-Earth Ions
·Atsushi Maeda and Hiroshi Sugimoto
·Journal of the Chemical Society, Faraday Transactions II, 82, 2019 (1986)

[4] ·Zeeman Effect on Anisotropic 4f Electron Systems
·Atsushi Maeda and Hiroshi Sugimoto
·Physica A, 144, 299 (1987)

[5] ·Composition Dependence of the Physical Properties in the Superconducting Y-Ba-Cu-O System
·Hiroyuki Tajima, Atsushi Maeda, Mototada Kobayashi, Tohru Satake, Hiromichi Shimada, Susumu Miyama and Haruo Kuroda
·Japanese Journal of Applied Physics, 26, L845 (1987)

[6] ·Nature of the 4f Spin in High T_C Superconductors Containing Paramagnetic Rare-Earth Elements $REBa_2Cu_3O_{7-y}$ (RE=Gd, Dy, Ho, Er and Tm)
·Atsushi Maeda, Hiroyuki Tajima, Tohru Satake, Haruo Kuroda, Takeji Takui and Koichi Itoh
·Journal of the Less-Common Metals, 139, 305 (1988)

[7] ·Relationship between Oxygen Deficiency and Superconductivity in $YBa_2Cu_3O_{7-y}$ Perovskite
·Hiromichi Shimada, Susumu Miyama, Hiroyuki Tajima, Atsushi Maeda, Tohru Satake, Mototada Kobayashi and Haruo Kuroda
·Journal of the Ceramic Society of Japan, 96, 392 (1988)

[8] ·高温超伝導体における常磁性種及び表面の超伝導磁気特性 － ＥＳＲ及び低磁場非共鳴マイクロ波吸収によるキャラクタリゼーション －
·前田篤志，黒田晴雄，工位武治
·表面科学，9, 521 (1988)

BY MOLECULAR BEAM EPITAXY TECHNIQUE

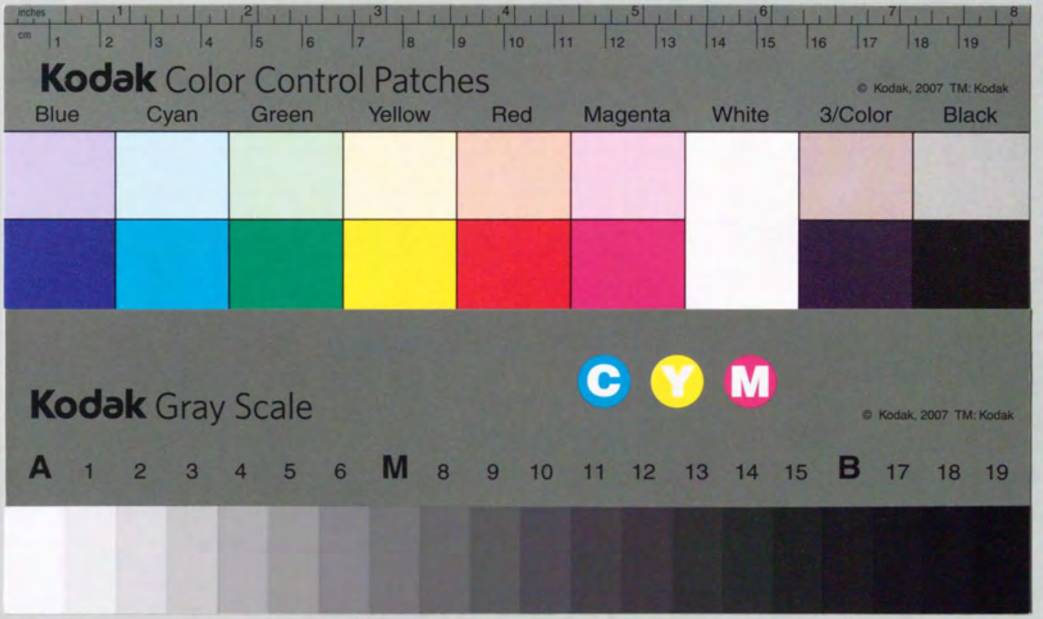
inches
cm
Kodak Color Control Patches
© Kodak, 2007 TM: Kodak
Blue
Cyan
Green
Yellow
Red
Magenta
White
3/Color
Black
Kodak Gray Scale
C
Y
M
© Kodak, 2007 TM: Kodak
A 1 2 3 4 5 6 M 8 9 10 11 12 13 14 15 B 17 18 19